INNOVATIONS IN ^{1}H MR TISSUE OXIMETRY:

NEW PROBES AND PULSES

by

UJJAWAL RASTOGI

Presented to the Faculty of the Graduate School of

The University of Texas at Arlington in Partial Fulfillment

of the Requirements

for the Degree of

MASTER OF SCIENCE IN BIOMEDICAL ENGINEERING

THE UNIVERSITY OF TEXAS AT ARLINGTON

DECEMBER 2010

ACKNOWLEDGEMENTS

It gives me immense pleasure and joy to thank all the people who supported and assisted me throughout the last year.

First, and foremost, I would like to thank my advisor Dr. Vikram D. Kodibagkar for allowing me to be a part of his team and pursue my research interest. I could not have hoped for a better person than Dr. Kodibagkar to guide me through my master's thesis. Dr. Kodibagkar has always encouraged me, motivated me, taught me and picked up me whenever I have fallen. His door was always open for me and no matter how busy he was, he had the patience of answering my questions whether professional or personal. Working with Dr. Kodibagkar was a lot of fun and no matter where I go, I will always miss working with him.

Dr. Ralph P. Mason has been a source of inspiration for me, the advice and suggestions he offers during our weekly lab meetings have helped me being a thinker. I would like to thank him, Dr. Roderick McColl and Dr. Georgios Alexandrakis for serving on my committee. I would also like to thank my fellow graduate students Praveen Gulaka and Sairam Geethanath. They have always advised me, helped me whether it is technical writing or MATLAB coding. They have been my best friends and have been my critics as well. They have always led me by examples and I think myself to be really fortunate to have them as my lab mates. I would also like to thank Jennifer Magnusson and Marisela Aguilera for assistance with cell culture and implantation. I would like to thank Dr. Xiankai Sun for allowing me to use his equipment for my experiments.

I extend my gratitude towards Dr. John M. Pauly, who unknowingly has been a very critical part of my thesis. I would like to thank him for his online course material through which I learned RF pulse design and related theory and also for publishing his MATLAB functions for RF pulse designing online.

My mother Malka Rastogi, father Azad Rastogi and my kid brother Shivam have been my biggest strength. I couldn't have done any of this without the love and support I got from them. I think whatever I am today is because of their dedication, sacrifice, and blessings. I would also like to thank my grandpa the Late Mr. Navneet Lal Rastogi and my grandmom the Late Mrs. Padma Devi for the love and blessings they have bestowed upon me.

November 15, 2010

ABSTRACT

INNOVATION IN ^{1}H MR TISSUE OXIMETRY:

NEW PROBES AND PULSES

Ujjawal Rastogi, MS

The University of Texas at Arlington, 2010

Supervising Professor: Vikram D. Kodibagkar

Low oxygenation level (hypoxia) of tissue leads to cellular dysfunction, damage and poor response to therapy. Quantitative measurement of tissue oxygenation is critical not only for the study of tissue physiology, but could also help improve efficacy of therapeutic procedures. Our group has previously developed and implemented a novel approach to quantify oxygen tension in tissue using ^{1}H MRI, known as "PISTOL" (**P**roton **I**maging of **S**iloxanes to map **T**issue **O**xygenation **L**evels). It exploits a linear relationship between the longitudinal relaxation rate (R_1) and oxygen tension (pO_2) of a reporter molecule (probe). Due to close proximity of fat (~ 1 ppm) and probe (~0 ppm) resonances there is a possibility of contamination of probe signal by spurious fat signal causing errors in quantification.

This study focuses on two aspects that are important to ^{1}H MR tissue oximetry 1) Characterization of new probes and 2) design and implementation of spatial spectral pulses for use with ^{1}H MR reporter molecules for improved lipid suppression. Several ^{1}H based pO_2 reporters and reporter molecule based nano emulsions (to facilitate systemic delivery) were characterized with respect to changes in oxygenation levels and temperature. This study included characterization of a) hexamethyldisiloxane (HMDSO) at 9.4 T and b)

hexamethyldisiloxane (HMDSO) based nanoprobes c) octamethyltrisiloxane (OMTSO) at 4.7 T and 9.4 T.

To further improve the PISTOL technique a single spatial spectral pulse (SPSP) has been designed and implemented that would enable selective examination of a particular slice and specified probe simultaneously without exciting signal from any other species in the slice. The work presented here has the potential to improve and extend the use of PISTOL for quantitative tissue oximetry.

TABLE OF CONTENTS

LIST OF ILLUSTRATIONS

Figure Page

LIST OF TABLES

Table Page

LIST OF ABBREVIATIONS

^{13}C	Carbon
^{15}N	Nitrogen
^{18}F-MISO	[18F] Fluoromisonidazole, 3-fluoro-1-(2'-nitro-1'-imidazolyl)-2-propanol
^{19}F	Fluorine
^{1}H	Proton
^{31}P	Phosphorous
99mTcHL91	99mTechnetium labeled 4, 9-diaza-3, 3, 10, 10-tetramethyldodecan-2, 11-dione dioxime
ADVARC	Alternating relaxation delays with variable acquisitions for reduction of clearance effects
B_0	Static or main magnetic field
B_1	Radio frequency excitation magnetic field
BOLD	Blood oxygen level dependant
BW	Bandwidth
CHESS	Chemical shift selective
DI-H2O	De-ionized water
DNA	Deoxyribonucleic acid
EM	Electromagnetic
EPI	Echo planar imaging
EPR	Electron paramagnetic resonance
FGF	Fibroblast growth factor
HIF	Hypoxia inducible transcription factor

HMDSO	Hexamethyldisiloxane
HS-15	Polyglycol mono-ester of 12-hydroxystearic acid
MRI	Magnetic resonance Imaging
NMR	Nuclear magnetic resonance
OMTSO	Octamethyltrisiloxane
PBS	Phosphate buffer saline
PDMS	Polydimethylsiloxane
PET	Positron emission tomography
PFC	Perfluorocarbons
PISTOL	Proton Imaging of siloxanes to map tissue oxygenation levels
pO_2	Partial pressure of oxygen
ppm	Parts per million
R_1	Spin-lattice or longitudinal relaxation rate
R_2	Spin-spin or transverse relaxation rate
RF	Radiofrequency
ROI	Region of interest
SLR	Shinnar Le-Roux
SPECT	Single photon emission tomography
SPSP	Spatial spectral pulse
TBW	Time bandwidth product
TI	Inversion Time
TR	Repetition time
VEGF	Vascular endothelial growth factor
PEG	Polyethylene glycol

CHAPTER 1

INTRODUCTION

1.1 Cancer and tumor microenvironment

Cancer is a class of diseases characterized by uncontrolled growth and spread of abnormal cells. It is one of the leading causes of death around the world. The American Cancer Society has estimated 569,490 deaths due to different types of cancer in 2010 in America alone (1). There are various strategies such as surgery, chemotherapy, radiation therapy, angiogenesis inhibitors therapy, bone marrow transplantation and peripheral blood stem cell transplantation, gene therapy, targeted cancer therapies, photodynamic therapy available for the treatment of cancer, though not all therapies are appropriate for all cancers. Of these chemotherapy and radiation therapy are most widely used treatments for cancer.

Physiologically, solid tumors are significantly different from normal tissue at the microenvironmental level. Most of these physiological differences are due to dissimilar vasculatures of the two tissue types (2). While normal tissue is characterized by regular, ordered vasculature with regulated blood supply, solid tumors on the other hand have abnormal vasculature which is chaotic and leaky with irregular, sluggish blood supply (3). Tumors recruit blood vessels through the process of neovascularization resulting from increased expression of proangiogenic factors produced by tumor cells. Tumor blood vessels are tortuous, have arterio-venous shunts, blind ends and have incomplete endothelial linings and basement membranes. This results in impaired oxygen delivery to tumors causing tumors to be highly heterogeneous with respect to oxygenation level and are often hypoxic (low oxygenation state) (4-6).

1.2 Hypoxia in tumors and its consequences

Hypoxia is a characteristic of tumor physiology/vasculature. Oxygen plays an important role in the well being of the tissue and hypoxia leads to cellular dysfunction and cell death (7). For most solid tumors hypoxia develops because of insufficient supply of oxygen to the growing tumor mass. The major factors which play an essential role in development of chronic (or diffusion-limited) hypoxia are abnormalities in structure and functioning of tumor vasculature, increased diffusion distances between blood vessels, growing tumor cell mass competing for oxygen and reduced oxygen carrying capacity of blood due to disease (8). It has been observed that tumor cells beyond 70 µm from the arterial end and 100 µm from the venous end of the capillary starve for oxygen. Acute (or perfusion-limited) hypoxia develops in tumors due to inadequate blood flow resulting from transient blockags of tumor neovasculature. Anaemic hypoxia occurs due to reduced oxygen carrying capacity of the blood (9).

Role of hypoxia in modifying the tumor microenviroment has been extensively reviewed in literature and hypoxia has been associated with many biological responses (10,11). In the absence of oxygen or at very low oxygenation level tumor cells undergo shift from aerobic to anaerobic glycolysis leading to accumulation of lactic acid which results in acidosis of tumor microenvironment thus reducing the efficacy of alkaline chemotherapeutic drugs (12,13). Hypoxia has also been associated with secretion of proangiogenic cytokines including vascular endothelial growth factor (VEGF) and fibroblast growth factor (FGF) that promote angiogenesis which further reduces the oxygen levels in the tumor cells (11). It has also been observed that hypoxia induces secretion of various growth factors known to promote cell proliferation. Hypoxia induces apoptosis through activation of two pro-apoptotic proteins NIX and NIP3 mediated by hypoxic response factor HIF-1α (11). Hypoxia also is seen to cause adaptive changes in the proteome and genome of neoplastic cells resulting in more aggressive clones of cancer cells which are resistant to treatment. Hypoxia has been proved to play a detrimental role in the efficacy of the therapeutic procedures (7,9,14). Pioneering work of Gray et al. (15)

showed the importance of presence of oxygen during irradiation in radiation damage. Ionizing radiation kills cells by breaking double strand of its DNA (Figure 1.1). Ionizations close to DNA produce a radical on DNA (denoted as DNA*). DNA* in the presence of oxygen gets oxidized to yield DNA-OO*, which fixes the damage. At critically low oxygenation levels the radical DNA* gets reduced by –SH containing compounds that restores the DNA* back to its original form DNA-H. Therefore, less DNA damage occurs in the absence of oxygen with tumor cells becoming more resistant to radiotherapy. Therefore determination of hypoxia in tumors is imperative for increasing efficacy of therapeutic procedures.

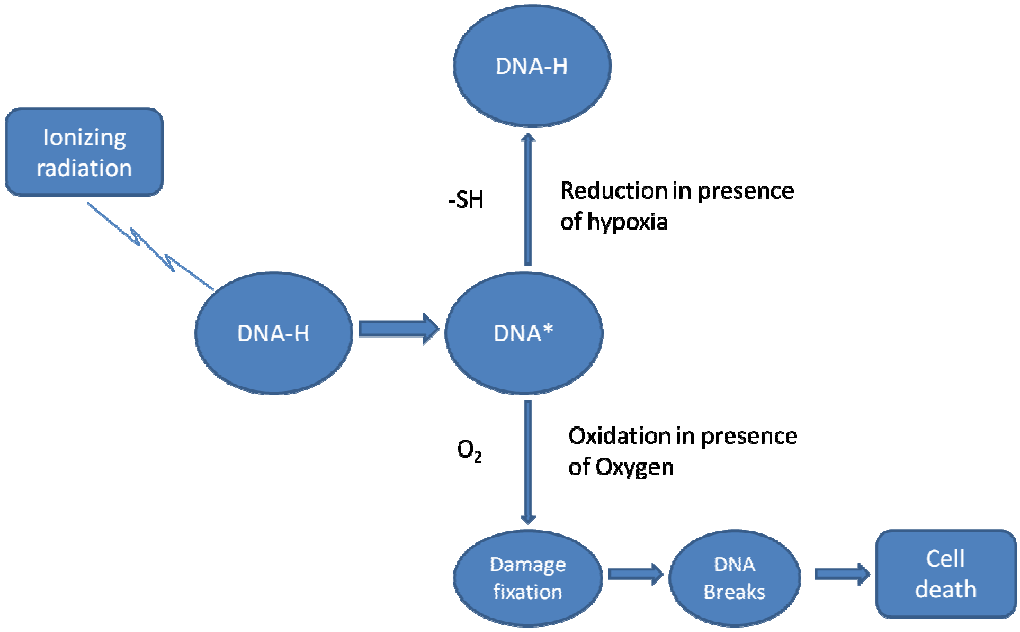

Figure 1.1: Importance of presence of oxygen at the time of irradiation. Presence of oxygen causes oxidation of DNA* making the damage permanent. In the absence of O_2 and presence of –SH containing compounds DNA* gets reduced to its original form DNA.

1.3 *In vivo* measurement of oxygen

Several techniques both qualitative and quantitative have been used for *in vivo* determination of tissue oxygenation (pO_2) (7,10,16).

Polarographic needle electrodes: This is a direct, quantitative and invasive method for the determination of tissue oxygenation and is considered to be a gold standard in the field (10,16-18). In this technique an anode is placed on the skin and is polarized with constant voltage. The polarographic needle electrode (cathode) is inserted into the tissue of interest and electrical current is generated proportional to the pO_2. Calibration of polarographic needle electrode is achieved by bubbling gases with varying composition of oxygen through phosphate buffered saline. Using this technique one can assess pO_2 at various locations simultaneously. The Eppendorf Histograph is an improved version of this technique wherein motion of needle is controlled by a computer and multiple measurements are made along tracks of tissues. The technique is sensitive to changes in pH, salinity and ionic strength. Consumption of oxygen at the tip of electrode might lead to errors in quantification. Due to invasive nature of the technique longitudinal studies are not possible.

Fiber optic probes: This is a direct, quantitative and invasive method which utilizes fiber optic oxygen sensors to assess tissue oxygenation (7,16,19,20). In this method an optical fiber carries light to the fluorophore coating at the tip of the probe. Oxygen in the tissue diffuses into the fluorophore coating and quenches the fluorescence. The fluorescence thus generated at the tip is returned by the optical fiber to a spectrometer. OxyLite™ and FOXY™ are two currently available commercial systems measuring fluorescent lifetime and fluorescent intensity respectively for quantitative determination of pO_2. Although there is no consumption of oxygen at the probe tip the fluorophore coating at the tip may wear off and needs to be re-applied time to time.

Positron emission tomography (PET): Several recent investigations have reported the use PET for qualitative determination of hypoxia non-invasively (21-23). The technique depends

upon selective accumulation of specially designed hypoxia targeting agents. [^{18}F]Fluoromisonidazole, 3-fluoro-1-(2'-nitro-1'-imidazolyl)-2-propanol (^{18}F-MISO) is an example of hypoxia targeted PET imaging agent. ^{18}F-MISO accumulates in the tissues by binding intracellular molecules when pO_2<10 mmHg. Imaging is accomplished in 20-30 minutes from 75 to 150 minutes after the injection. Many such agents have been extensively reviewed in literature. Limitations of PET include modest signal to noise of raw PET images, low spatial resolution, and qualitative nature of technique.

Single photon emission computed tomography (SPECT): SPECT imaging agents have been developed which can also give qualitative assessment of hypoxia (24)**.** The principle of this technique is similar to PET where imaging agents gets accumulated in hypoxic regions of tissue. PET usually has higher sensitivity and is 100 times more sensitive than SPECT. ^{99m}Technetium labeled 4, 9-diaza-3, 3, 10, 10-tetramethyldodecan-2, 11-dione dioxime (^{99m}Tc HL91) is a SPECT imaging agent with a 6 hours half life. The technique has limitations similar to PET.

Magnetic resonance based methods

MRI and NMR methods can be used for both qualitative and quantitative determination of oxygenation levels (7,16,22,25).

BOLD-MRI: Blood Oxygen Level Dependant (BOLD) is a qualitative technique for the assessment of hypoxia. Tissue contrast in BOLD images (changes in R_2*) results from paramagnetic deoxy-haemoglobin within red blood cells and hence reflects vascular oxygen saturation. Contrast of BOLD image is influenced by hematocrit, vascular volume, and flow. Since the changes in BOLD signal are sensitive to changes in vascular oxygenation, correlation of signal changes with tissue pO_2 are relative and not absolute.

Electron paramagnetic resonance (EPR): While NMR signal relies on the non-zero nuclear spin of particular nuclei EPR signal is dependent upon unpaired electrons although both result from the Zeeman interaction of spin with external magnetic fields. Paramagnetic oxygen causes

changes in electronic spin-lattice and spin-spin relaxations of other paramagnetic species. Changes in relaxation rate are observed as changes in EPR linewidth which is proportional to concentration of oxygen. Reporter molecules can be administered either intratumoraly or intravenously. The technique has been extensively reviewed in literature (26-29). One of the important drawback of this technique is the lack of widespread EPR instrumentation for pre clinical and clinical investigations.

Magnetic resonance oximetry: MR oximetry has been extensively used for quantitative determination of pO_2 (7,16,30,31). In this technique reporter molecules are administered either intratumoraly or intravenously. Paramagnetic oxygen relaxes the nuclear spins of the reporter molecule. Thus, by determining intrinsic properties of a molecule such as spin-lattice relaxation rate one can quantitatively determine oxygen tension in the tissue. Perfluorocarbons (PFC) such as hexafluorobenzene have been investigated previously and have demonstrated excellent capabilities for quantitative determination of pO_2. PFC based MR oximetry has a limitation due to lack of widespread instrumentation available for ^{19}F MRI. Recently, Kodibagkar et al.(32) demonstrated the potential and capability of a siloxane based pO_2 reporter molecule for quantitative determination of pO_2 using ^{1}H MRI.

1.4 Principles of MR excitation

MRI principles can often be accurately described using classical vector model because of the collective behavior of huge number of nuclei present in the macroscopic object, although the true description of the phenomenon is quantum mechanical in nature. NMR signal is generated by nuclei that possess an overall spin (^{1}H, ^{13}C, ^{31}P, ^{15}N, ^{19}F, etc) and radiate absorbed energy from electromagnetic pulse (EM) when placed in a static magnetic field B_0.

In the presence of strong static magnetic field these spins get polarized and produce a net magnetization (also referred to as bulk magnetization) along the direction of static field precessing at angular frequency of ω_0. It should be noted that at thermal equilibrium spins along the transverse plane have no phase coherence giving zero transverse magnetization. Since

NMR signal cannot be observed along the direction of applied magnetic field, magnetization has to be flipped into the plane transverse to the static magnetic field. The process of perturbing the thermal equilibrium and establishing phase coherence with an external radio frequency (RF) excitation field B_1 oscillating at frequency ω_1 is known as excitation (33) . The amount of magnetization flipped into the transverse plane is determined by the flip angle of the RF pulse. Mathematically flip angle can be defined as

$$\theta = \gamma \int_0^T B_1(t) \qquad [1]$$

where θ is the flip angle in radians, γ is the gyromagnetic ratio and is different for different nuclei and T is the duration of the pulse. Resonance condition is met when the frequency of the applied RF field B_1 matches the frequency at which the nuclear spins are precessing (also known as Larmor frequency) that is when $\omega_1=\omega_0$. Specifically B_1 field is turned on for a few microseconds or milliseconds. Also, the B_1 field is much weaker (in order of mT) than the static magnetic field. When B_1 field is turned off nuclear spins tend to align themselves along the main magnetic field. The rate at which the longitudinal component of the magnetization (M_z) grows is known as spin-lattice or longitudinal relaxation rate R_1 ($1/T_1$), while the rate at which the transverse component of the magnetization (M_{xy}) decays is known as spin-spin or transverse relaxation rate R_2 ($1/T_2$). In general, B_1 field at the resonant frequency excites the whole volume inside the coil. Magnetic field gradients (G_x, G_y or G_z) are used in conjunction with B_1 field for selective excitation of a small portion of volume, for example a slice, a cylinder or a cube.

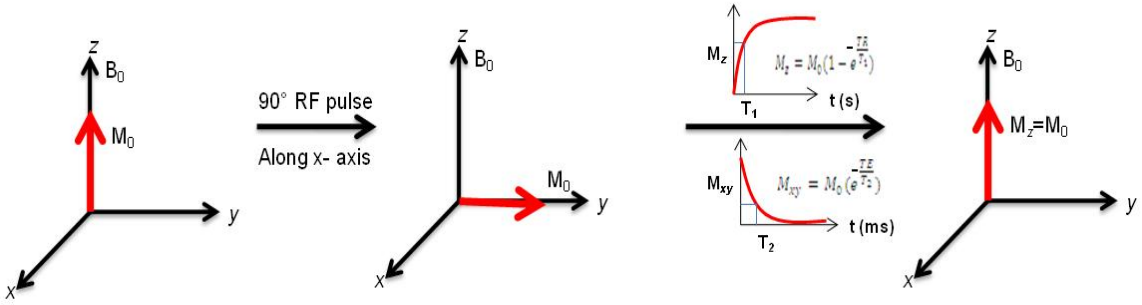

Figure 1.2: Effect of 90°RF pulse on the magnetiza tion. Once the RF is switched off longitudinal magnetization tends to grow with time constant T_1 and transverse magnetizations decays with a time constant T_2.

1.4.1. 2D radiofrequency (RF) pulses

2D RF pulses excite magnetization in more than one direction. A 2D spatially selective RF pulse requires two time varying slice select gradients played simultaneously on two independent gradient axes (34). While a conventional 1D pulse excites a slice of magnetization, 2D RF pulses on the other hand can excite either a cylinder or a long strip depending upon the type of slice selective gradients (spiral or trapezoidal) used. 2D RF pulses can be designed using the k-space analysis (35) for small flip angles or by iterative/SLR methods (34,36).

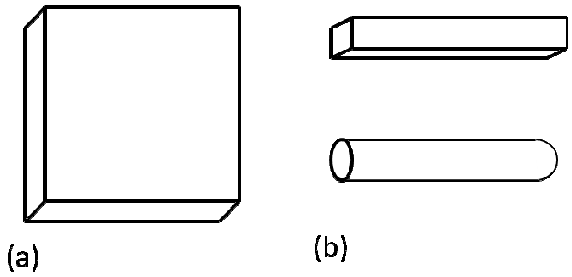

Figure 1.3: Representation of the spatial profiles excited by RF pulses. (a) A standard 1D RF pulse excites a slab, (b) A 2D pulse either excites a long strip or a cylinder depending upon the functional form of slice select gradient.

*1.4.2 **k** space analysis of small-tip-angle selective excitation*

Pauly et al.(35) introduced a k space approach to interpret the selective excitation by a small flip angle (θ<=30º) RF pulse using well known small -tip approximation. Though the

interpretation is valid only for pulses in small flip angle regime, it holds well for flip angles on the order of 90°. They suggested excitation by a RF pulse in magnetic resonance imaging can be analyzed as scanning a path in a spatial frequency space or k space.

According to Pauly et al., neglecting T_1 and T_2 relaxations, the time dependant behavior of magnetization in presence of excitation field B_1 ($B_{1,x}$, $B_{1,y}$) and magnetic field gradient G (G_x, G_y, G_z) is governed by Bloch equation given as

$$\frac{d}{dt}\begin{pmatrix} M_x \\ M_y \\ M_z \end{pmatrix} = \gamma \begin{pmatrix} 0 & G.r & -B_{1,y} \\ -G.r & 0 & B_{1,x} \\ B_{1,y} & -B_{1,x} & 0 \end{pmatrix} \begin{pmatrix} M_x \\ M_y \\ M_z \end{pmatrix} \quad [2]$$

Bloch equations can be solved using the well known small-tip-angle approximation to yield the following expression for the transverse magnetization

$$M_{xy}(\boldsymbol{r}) = i\gamma M_0(\boldsymbol{r}) \int_{\mathrm{k}} W(\mathbf{k}) S(\mathbf{k}) e^{i\boldsymbol{r}.\boldsymbol{k}} d\mathbf{k} \quad [3]$$

where

$$W\big(\mathbf{k}(t)\big) = \frac{B_1(t)}{\left|\dot{\mathbf{k}}(t)\right|} \quad [4]$$

$$S(\mathbf{k}) = \int_{\mathbf{0}}^{\mathbf{T}} \{^3\delta(\mathbf{k}(t) - \mathbf{k}) \left|\dot{\mathbf{k}}(t)\right|\} dt \quad [5]$$

$$\mathbf{k}(t) = -\gamma \int_{\mathbf{t}}^{\mathbf{T}} G(s) ds \quad [6]$$

and

$$\left|\dot{\mathbf{k}}(t)\right| = \frac{d}{dt}\mathbf{k}(t) \quad [7]$$

Thus the transverse magnetization is the product of initial magnetization and the inverse Fourier transform of a spatial frequency weighting function *W*(**k**) in a three dimensional k space multiplied by a spatial frequency sampling function *S*(**k**). The factor $\left|\dot{\mathbf{k}}(t)\right|$ is included to normalize the delta function and to obtain explicit weighting of k space by $B_1(t)$. To design a 2D

spatially selective RF pulse the pulse designer first needs to choose appropriate gradients such that S(**k**) completely and uniformly sample the spatial frequency space. Then one can choose W(**k**) as the Fourier transform of the desired transverse magnetization. Corresponding $B_1(t)$ can be determined using Equation [4].

1.4.3 Spatial spectral pulses

Instead of using two separate RF pulses to achieve spectral and spatial selectivity a single spatial spectral RF pulse (37) is used to achieve simultaneous spatial and spectral selectivity. A spatial spectral pulse can excite magnetization from one species (e.g., probe) without affecting the magnetization from other species (e.g., water and fat) at a particular location within the entire volume. Beside excitation, spatial spectral pulses can be also employed for saturation of MR signal. Spatial spectral RF pulses are 2D RF pulses with space and frequency as its two dimensions and are designed in the same way as 2D spatially selective pulses. Since we want to design a pulse which is simultaneously selective in the slice selection direction, z, and spectral direction, ω the corresponding k space axis can be defined as

$$\mathbf{k}_z(t) = -\gamma \int_{\mathbf{t}}^{\mathbf{T}} G(s)ds \qquad [8]$$

$$\mathbf{k}_\omega(t) = \mathrm{t} - \mathrm{T} \qquad [9]$$

Equation [8] implies that $\mathbf{k}_z$ ranges over the time remaining in the interval and ends at origin as opposed to readout k space where **k** trajectory starts at origin. Equation [9] implies that traversal in spectral dimension is achieved by simply waiting in time. Since $\mathbf{k}_\omega$ moves linearly with time $\mathbf{k}_z$ must oscillate in order to produce sampling of excitation k space.

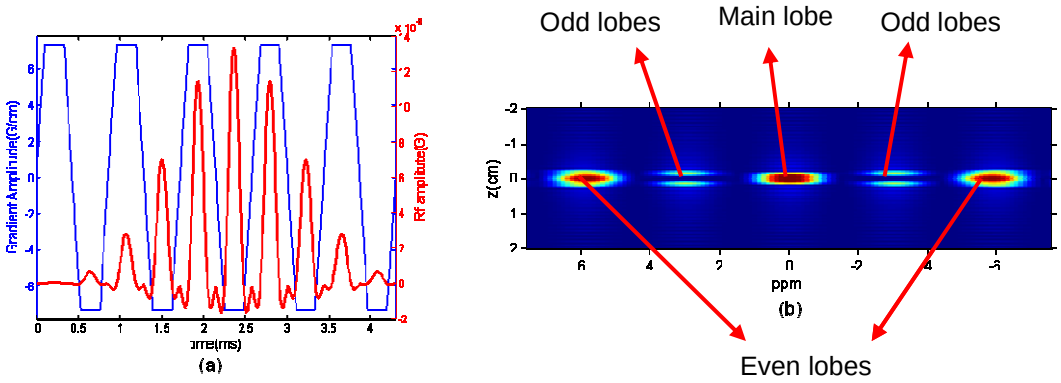

Figure 1.4: A spatial spectral pulse and corresponding magnetization response.(a) A 4 ms spatial spectral pulse with sub lobe duration of 0.43 ms (red) and spectral bandwidth 500 Hz played in conjunction with oscillating gradients (blue) to produce a slice of thickness 3 mm, (b) Corresponding magnetization response of the pulse. Main lobe appears at z=0, ω=0, even lobes appear at every 1/0.43 ms = ± 2.3 kHz from subsequent lobe (at 9.4 T ~ 5.75ppm). Odd side lobes appear halfway between the main lobe and even lobes.

Spatial spectral pulses consist of multiple RF sub pulses that are played under a broad RF envelop in conjunction with an oscillating gradient. These sub pulses along with bi-polar oscillating slice select gradients add spatial selectivity, whereas the RF envelop determines the spectral bandwidth of the excitation. From the small–tip-angle approximation we know the transverse magnetization excited is the inverse Fourier transform of the applied $B_1(t)$. Then for a train of RF subpulses separated by ΔT and played during both negative and positive gradient lobe the transverse magnetization excited is separated by $1/\Delta T$. Thus, the magnetization response of a spatial spectral pulse has a main peak at on resonance frequency (ω=0) as well as its periodic replicates (also known as even side lobes). Odd side lobes exist halfway between main lobe and even side lobes, odd side lobes result from eddy currents and RF/gradient delays. Odd side lobe structure is such that the total magnetization excited by them integrates to zero.

In the following chapters I will be discussing characterization of such ^1H based pO_2 reporter molecules which can be used for quantitative determination of tissue pO_2. I will also discuss the design and implementation of some probe specific spatial spectral RF pulses which would aid in selective imaging of such pO_2 reporter molecules.

CHAPTER 2

PROBES FOR QUANTITATIVE ^{1}H MR TISSUE OXIMETRY

2.1 Principles of quantitative MR oximetry

Quantitative MR oximetry exploits physical interactions between oxygen and reporter molecules. Probes used for MR oximtery must preferably possess the following characteristics: high oxygen solubility, hydrophobicity (so that diffusion of aqueous ions is restricted), should have a single resonance so that there are no chemical shift artifacts in the MR images and minimal dependence of R_1 on temperatures. Due to paramagnetic nature of molecular oxygen it tends to shorten the nuclear relaxation times and relaxes the nuclear spins faster thereby increasing the spin-lattice and spin-spin relaxation rate R_1 and R_2 respectively of the reporter molecule. The principle is based on linear dependence of pO_2 on the spin lattice (longitudinal) relaxation rate of the probe ($R_1=1/T_1$). In order to understand the principle in detail, assume that the pO_2 probe is injected into the tissue where it can be divided between two pools of molecules, (1) molecules that have oxygen in their vicinity, (2) and molecules that don't have oxygen in their vicinity. Due to high solubility of oxygen in the reporter agent, the observed relaxation rate for each pool of probe is a molar weighted average. If x is the molar fraction of oxygen the net relaxation rate can be defined as

$$\boldsymbol{R_1 = (1-x)R_{1d} + x^*\left(R_{1d} + R_{1p}\right) = R_{1d} + x^*R_{1p}} \qquad [10]$$

Where R_1 = net relaxation rate of the probe.

R_{1d} = anoxic component of the relaxation rate.

R_{1p} = Paramagnetic component of the relaxation rate due to contribution of oxygen. As per Henry's law, the dissolved mole fraction is directly related to the partial pressure of oxygen.

$$\boldsymbol{pO_2 = k^* x} \quad [11]$$

k is a constant that determines the solubility of oxygen in the agent and is different for different agents. Thus net relaxation rate becomes

$$\boldsymbol{R_1 = A' + B'^* pO_2} \quad [12]$$

where A' = R_{1d} and B' = R_{1p}/k

Since longitudinal relaxation rate is a function of temperature we assume a linear dependence of constants A' and B' on temperature (for relevant physiological range) which emperically can be defined as

$$\boldsymbol{A' = A + C^* T} \quad [13]$$

$$\boldsymbol{B' = B + D^* T} \quad [14]$$

Substituting value of A' and B' in Equation [12] results in a temperature dependent model for net relaxation rate

$$\boldsymbol{R_1 = A + B^* pO_2 + C^* T + D^* T^* pO_2} \quad [15]$$

Using above equation oxygenation levels can be determined quantitatively leading to more accurate and reliable quantification. At the very least, errors in pO_2/℃ at a particular oxygenation level or temperature can be determined. Therefore estimation of these parameters is very important.

2.2 Materials and Methods

2.2.1 In vitro calibration experiments

Calibration experiments were performed to characterize the dependence of R_1 on pO_2 and temperature and to extract characterization parameters A, B, C, and D. 200 µL of agent was put in a gas tight NMR tube (Wilmad-Labglass; Buena, NJ, USA). Gases used for calibrating a probe contained 0%, 5%, 10% and 21% oxygen and rest nitrogen (Air Gas, Dallas, TX, USA). Gases with varying oxygen concentrations were made by mixing nitrogen and air in varying proportions in a HypoxyDial™ (STARR Life Sciences Corp.; Oakmont, PA, USA). A pO_2 meter was connected in line with the output of the HypoxyDial™ in order to verify accuracy of the HypoxyDial™. Output gas from the HypoxyDial was connected to an inflatable glove bag (Glas-Col; Terre Haute, IN, USA) consisting of internal gloves, inlet through which gas tube from HypoxyDial™ enters and an equipment sleeve. NMR tube containing agent was kept inside the Glove bag through equipment sleeve and the bag was closed. Gas from the HypoxyDial™ was allowed to inflate the glove bag and was purged when bag was almost full. The glove bag was purged three times, fourth time the gas was filled but not flushed out, this was done in order to flush out air (which had different oxygen concentration) and create an environment of only desired gas inside the bag . The tube from the HypoxyDial™ was then connected to another tube of much smaller diameter without opening the glove bag, the other end of the tube was put in the NMR tube and the flow rate was adjusted to obtain slow bubbling of the agent. Agent was bubbled for 15 minutes and after bubbling the NMR tube was sealed inside the glove bag.

2.2.2 NMR experiments

NMR experiments were performed on a Varian Inova 4.7 T or 9.4 T horizontal bore pre clinical scanner equipped with actively shielded gradients.

A spin-echo-based pulse sequence was used for spectroscopic determination of T_1 for experiments carried on 4.7 T system (see figure2.1). The sequence was implemented by my

mentor Dr. Vikram D. Kodibagkar and has been employed previously for determination of T_1 of HMDSO (38). Basically the pulse sequence consists of 20 nonselective π/2 saturation pulses with interpulse delay of 50 ms (pulse-burst saturation recovery), followed by a variable delay τ for magnetization to recover as originally developed by Markley et al.(39). Three optional chemical shift selective (CHESS) pulses at the end of τ can be used for saturation of residual water and fat resonances. After τ, frequency selective gaussian π/2 and π pulses were applied. Echo time of 100 ms was used which helped in suppression of the fat resonance. T_1 determination was accomplished using this sequence with ADVARC (alternating relaxation delays with variable acquisitions for reduction of clearance effects) protocol, by using τ values of 0.1, 0.2, 0.4, 0.8, 1.2, 2, 3, 3.5, 4, 5, 6, 8, 12.5, 20, 40, 55 s. The total acquisition time to obtain one T_1 value was around 3 minutes. Five such measurements were performed, mean and standard deviation of those five measurements was considered while plotting the acquired data. Home built 1cm diameter surface coil was used for these experiments. T_1 of the probe was measured as function of temperature in the physiologically relevant range and was varied from 22℃ to 52℃. In order to heat the sample, NMR tube was covered by a pad through which hot water was circulated. A fiber optic temperature sensor (FISO Technologies Inc., Quebeck, Canada) was used to monitor the temperature of the NMR tube. All experiments other than those investigating temperature dependence were done at 37℃.

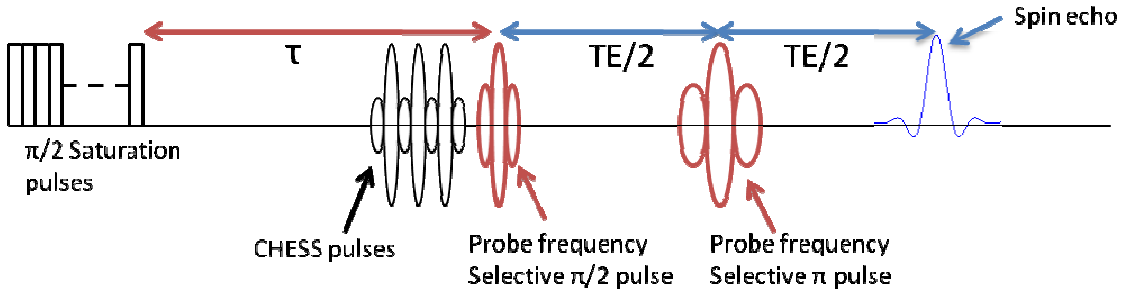

Figure 2.1: s2pulecho pulse sequence with optional CHESS pulses to suppress water and fat used for mapping T_1 on a 4.7 T scanner.

Calibration of a few probes was also carried out on 9.4 T systems. An existing inversion recovery based pulse sequence was used to measure T_1 of the probe (see figure 2.2). Basically the pulse sequence consisted of an initial delay followed by 180° inversion pulse (hard pulse). Following 180° pulse the magnetization was allowed to recover for a time d2 or TI (inversion time) and the residual magnetization was examined by a 90° hard pulse. An array of d2 values was used to cover exponential relaxation of the magnetization with TR=50 sec. d2 values used were 0.2, 0.3, 0.5, 0.8, 1, 2, 5, 7, 10, 20, 49 seconds respectively. It took around 9 minutes to obtain one T_1 value, three such measurements were done and mean of those three values was considered while plotting the acquired data. A 38mm inner diameter volume coil (Varian Inc.) was used in these experiments. To measure R_1 dependence on temperature the temperature of NMR tube was varied using a hot air blower. A temperature sensor was taped to the tip of NMR tube to monitor the temperature. Measurements were done when temperature was stable for 5 minutes to ensure that the agent inside the NMR tube reached the desired temperature.

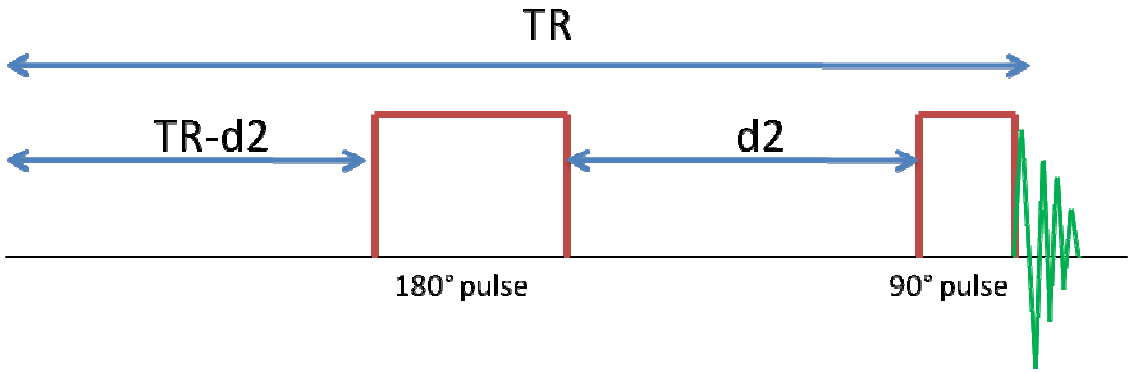

Figure 2.2: Inversion recovery based pulse sequence used for estimating T_1 values on a 9.4 T scanner.

The T_1 data obtained at 4.7 T and 9.4 T systems was fit to a single exponential, three parameter saturation ($A=M_0$, $B=M_0$, $C=\tau$; refer Equation [16]) and inversion ($A=M_0$, $B=2*M_0$, C=d2 or TI, refer Equation [16]) recovery equation respectively using the Levenberg-Marquardt algorithm with VNMR6.1C (4.7 T) and VNMRj (9.4 T) software on Varian scanners. Three parameter fit

provides a robust and highly accurate fit to the supplied data and corrects for any deviations from actual 90° or 180° pulse.

$$M_z = M_0 (1 - e^{-\frac{\tau}{T_1}}) \quad [16]$$

2.2.3 Synthesis of nanoemulsions

Due to hydrophobic nature of the probes they do not mix in blood directly and therefore cannot be used for systemic (intravenous) delivery. To facilitate systemic delivery of the probe biocompatible emulsions were synthesized to accomplish *in vivo* studies. “Oil in water” type emulsions were made with HMDSO (Sigma Aldrich, St Louis, Mo, USA) used as oil phase. HS-15, PEGylated (molecular weight 600 and 3000) were used as surfactant for various formulations. HS-15 was a gift from BASF Corporation and PEG-PDMS (molecular weight 600, 3000) was purchased from Polysciences, Inc. Warrington, PA, USA. For preparation of nanoemulsions de-ionized water or phosphate buffer saline (PBS) was added to the mixture of emulsifier and probe. The mixture was made in a glass bottle and the bottle was kept in an ice bath. Sonication was performed for 15 minutes, using Omniruptor 4000 Ultrasonic Homogenizer (Omni International, Kennesaw, GA, USA) at 150 W output power and 50% duty cycle. To achieve further reduction in particle size, emulsions were filtered using LiposoFast® extrusion filter (Avestin Inc., Ottawa, Canada) with a polycarbonate membrane filter of 100 nm pore size. Particle sizes were measured before and after filtration of emulsion using a Wyatt Technologies Gynapro Titan (Wyatt Technology Corporation, Santa Barbara, CA, USA) dynamic light-scattering instrument.

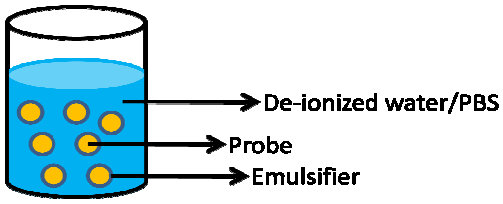

Figure 2.3: Diagrammatic representation of oil in water type emulsion.

2.3 Results

2.3.1 Calibration of HMDSO at 4.7 T

Calibration of HMDSO was done at 4.7 T using method described earlier. R_1 values were obtained as a function of pO_2 while temperature was kept constant at 37℃ (see figure 2.4). The acquired data was fit to a linear model and was compared to the data obtained previously by my mentor Dr. Kodibagkar (38). My experiment yielded calibration constants A' = 0.1167 ± 6.6x10^{-4}s^{-1} and B'=0.0012 ± 1.89x10^{-5}) (Torr*s)$^{-1}$, with R^2=0.9867. Including 760 Torr point for fitting resulted in a better fit (R^2=0.999) and reported calibration constant A' = 0.1141 ± 5.36x10^{-4} s^{-1} and B'=0.0013 ± 5.5x10^{-5} (Torr*s)$^{-1}$. Previous experiment data reported calibration constant A' = 0.1122 ± 0.001 s^{-1} and B'=.0013 ± 1.59x10^{-5} (Torr*s)$^{-1}$, without 760 Torr point. and A' = 0.1125 ± 0.0014 s^{-1} and B'=0.0013 ± 2.09x10^{-5} (Torr*s)$^{-1}$ (with 760 Torr point included).

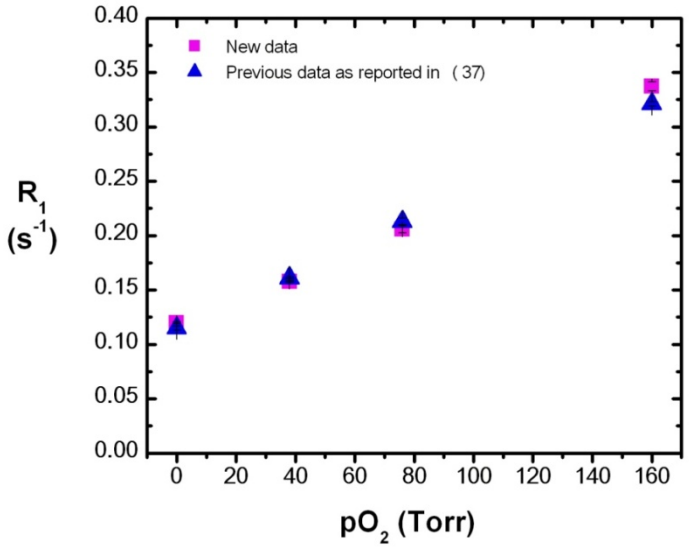

Figure 2.4: R_1 dependence on pO_2 at 37^{o}C at 4.7 T for neat HMDSO. Fitting data to a linear model resulted in calibration equation R_1= 0.1167 ± 6.6x10^{-4} + 0.0012 ± 1.89x10^{-5}* pO_2 and R_1= 0.1122 ± 0.001 + 0.0013±1.59x10^{-5} * pO_2 for new and previous data respectively.

2.3.2 Calibration of HMDSO at 9.4 T

Calibration of HMDSO was done at 9.4 T to study the effect of variation of pO_2 and temperature on R_1 of HMDSO using methods described earlier. Acquired data was fitted to a linear model and constants A' and B' at different temperatures were extracted. Since constants A' and B' are assumed to be linearly dependent upon temperature, A' and B' were plotted with respect to variations in temperature in the physiologically relevant range of 17℃ to 42℃ to yield characterization parameters A= 0.1621 ± 3.45×10^{-4} s^{-1}, B= 0.0015 ± 8.17×10^{-6} $(s*Torr)^{-1}$, C= -0.0014 ± 1.77×10^{-5} $(s*℃)^{-1}$, D= -7.75×10^{-6} ± 3.5×10^{-7} $(s*Torr*℃)^{-1}$ for neat HMDSO at 9.4 T.

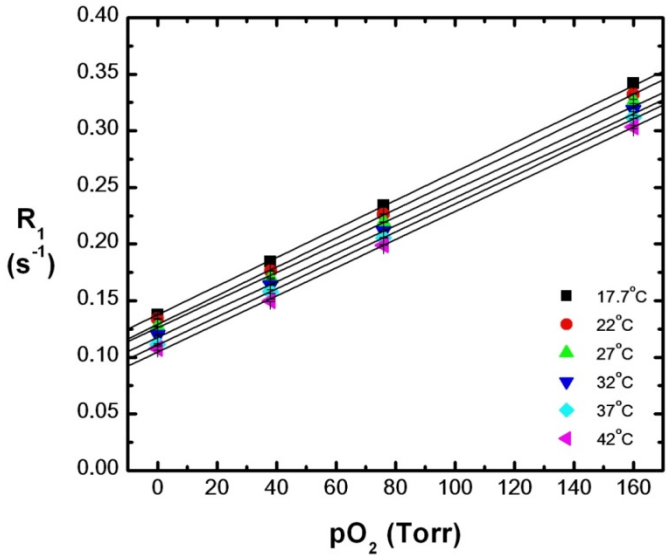

Figure 2.5: R_1 dependence on pO_2 at different temperatures on a 9.4 T scanner for neat HMDSO.

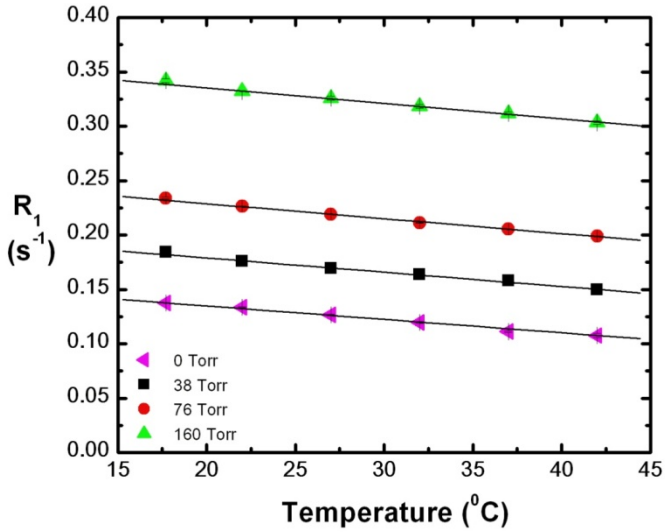

Figure 2.6: Neat HMDSO R_1 dependence on temperature at various pO_2 levels on a 9.4 T scanner.

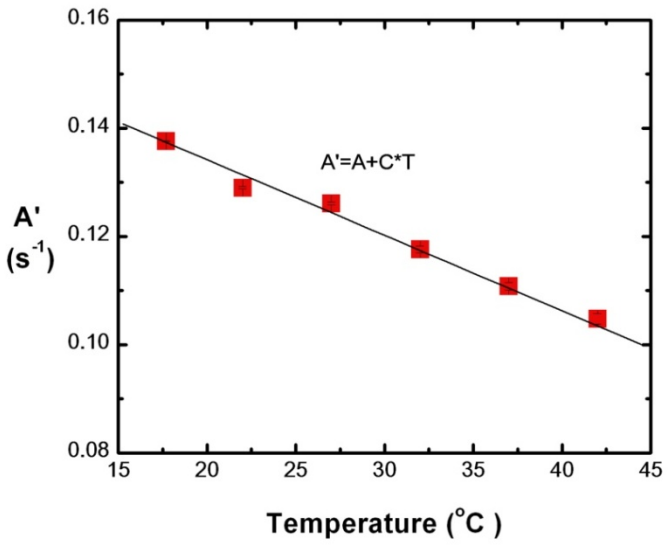

(a)

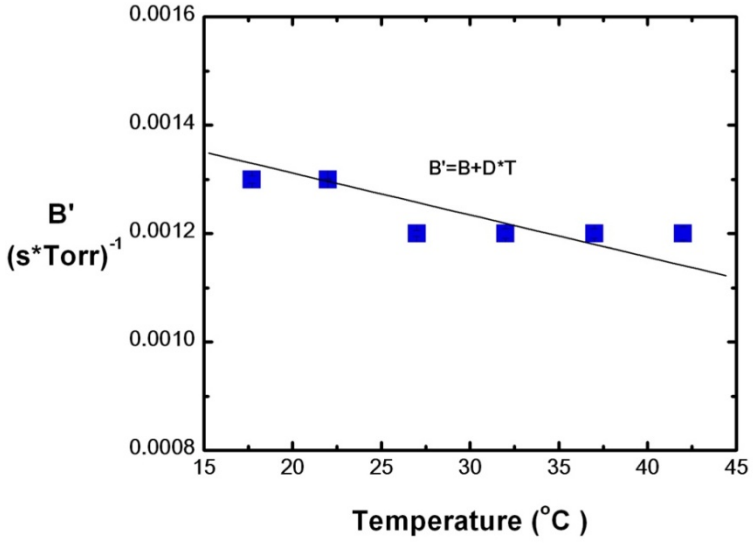

(b)

Figure 2.7: Neat HMDSO temperature dependence of constant (a) A' and (b) B' at 9.4 T. Fitting data to a linear model resulted in calibration constant (a) A= 0.1621 ± 3.45x10^{-4} s^{-1}, C= -0.0014 ± 1.77x10^{-5} (s*℃) $^{-1}$, and (b) B= 0.0015 ± 8.17x10^{-6} (s*Torr)$^{-1}$ and D= -7.75x10^{-6} ± 3.5x10^{-7} (s*Torr*℃) $^{-1}$ respectively.

Using the characterization parameters A, B, C, D relative errors introduced in pO_2 determination were calculated at 4.7 T and 9.4 T. 4.7 T data was taken from (38). Empirically error in pO_2 determination for change in temperature by 1℃ at a particular temperature T and oxygenation level pO_2 can be written as:

$$\frac{\Delta \boldsymbol{pO_2}}{\Delta \boldsymbol{T}} = \frac{|\boldsymbol{C} + \boldsymbol{D^* pO_2}|}{\boldsymbol{B} + \boldsymbol{D^* T}} \qquad [17]$$

Using above equation errors in pO_2 determination were calculated for oxygenation levels in relevant hypoxic range (0 Torr to 50 Torr) at 37℃ for a change in temperature by 1℃.(figure). For pO_2 of 5 Torr, resulting error in pO_2 determination for change in temperature by 1℃ at 37℃ was ~ 1.18 Torr/℃ at 9.4 T and was ~ 0.76 Torr/℃ at 4.7 T

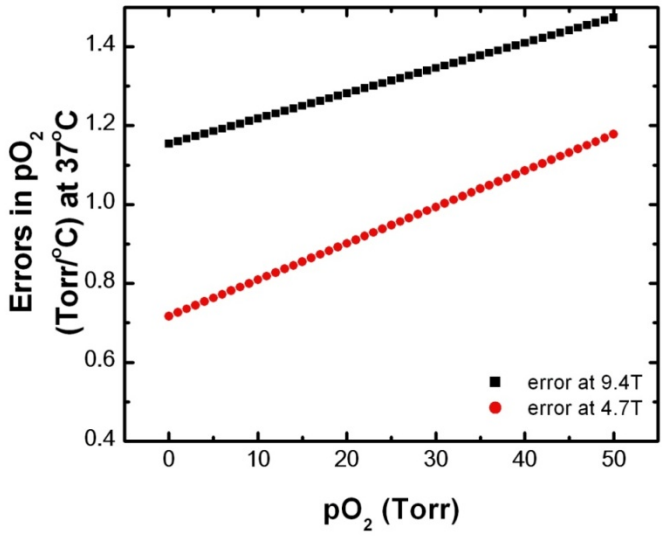

Figure 2.8: Comparison of simulated error in pO_2 determination for neat HMDSO with 1°C change in temperature in hypoxia relevant pO_2 range at 37°C at 4.7 T and 9.4 T.

2.3.3 Calibration of HMDSO based nanoemulsions

Three HMDSO based nanoemulsions were formulated and calibrated on a 4.7 T system to study the effect of pO_2 on their R_1: a) 2% v/v PEG-PDMS (600): 30% v/v HMDSO, b) 2% v/v PEG-PDMS (600): 40% v/v HMDSO and c) 5% v/v HS-15: 40% HMDSO in phosphate buffer saline (PBS). Table 2.1 summarizes A' and B' values obtained from the experiment.

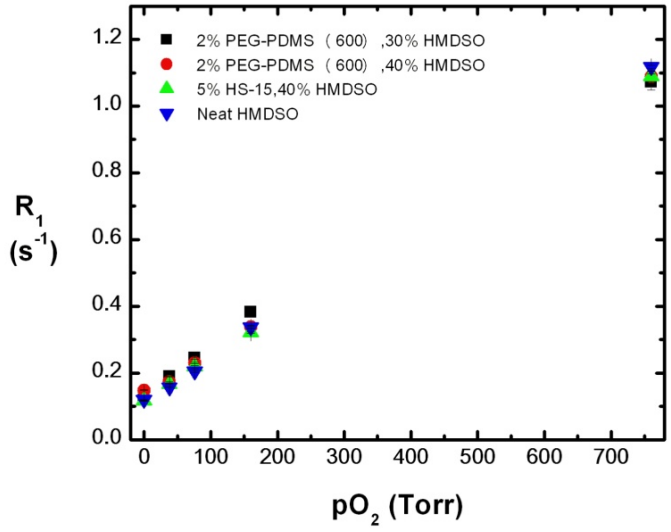

Figure 2.9: R_1 dependence on pO_2 for various nanoemulsions compared with neat HMDSO at 37°C on a 4.7 T scanner

Table 2.1: Calibration constants A' and B' for various nanoemulsions and neat HMDSO.

Probe	**A'** **(s^{-1})**	**B'** **$(s*Torr)^{-1}$**
2% v/v PEG-PDMS (600),30% v/v HMDSO rest PBS	0.1249 ± 0.0011	$0.0015 \pm 2.5x10^{-5}$
2% v/v PEG-PDMS (600),40% v/v HMDSO rest PBS	0.1426 ± 0.001	$0.0012 \pm 1.5x10^{-5}$
5% v/v HS-15, 40% HMDSO rest PBS	0.1181 ± 0.0013	$0.0013 \pm 1.2x10^{-5}$
Neat HMDSO	$0.1141 \pm 5.36x10^{-4}$	$0.0013 \pm 5.5x10^{-5}$

Due to high oxygen sensitivity and reduced particle size of 5% v/v HS-15, 40% v/v HMDSO rest DI-H_2O provided (40), it was further used to study effect of temperature on its R_1 at 4.7 T system. Characterization parameters A= 0.1699 ± 0.0016 s^{-1}, B= 0.0016 ± 4.53x10^{-5} $(s*Torr)^{-1}$, C= -0.0013 ± 4.53x10^{-5} $(s*℃)^{-1}$ and D = -1.25x10^{-5} ± 1.008x10^{-6} $(s*Torr*℃)^{-1}$ were determined. R_1 dependence of 5% v/v HS-15, 40% v/v HMDSO rest PBS on temperature and pO_2 was carried out (A= 0.1653 ± 0.0022 s^{-1}, B= 0.0014 ± 2.34x10^{-5} $(s*Torr)^{-1}$, C= -0.0013 ± 6.38x10^{-5} $(s*℃)^{-1}$, and D= -5x10^{-6} ± 7.3x10^{-7} $(s*Torr*℃)^{-1}$) to see if changes in the water phase of the emulsion causes any changes to the oxygen and temperature sensitivity of the probe. At a pO_2 5 Torr, error in pO_2 determination for change in temperature by 1℃ at 37℃ was ~ 1.2Torr/℃ for 5% v/v HS-15, 40% v/v HMDSO rest DI-H_2O and was ~ 1.1 Torr/℃ for 5% v/v HS-15, 40% v/v HMDSO rest PBS.

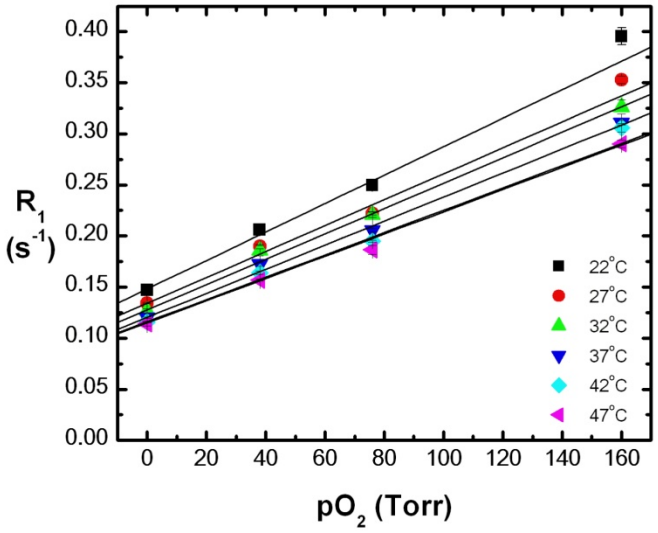

Figure 2.10: 5% v/v HS-15, 40% v/v HMDSO, 55% v/v DI-H_2O R_1 dependence on pO_2 at 4.7 T.

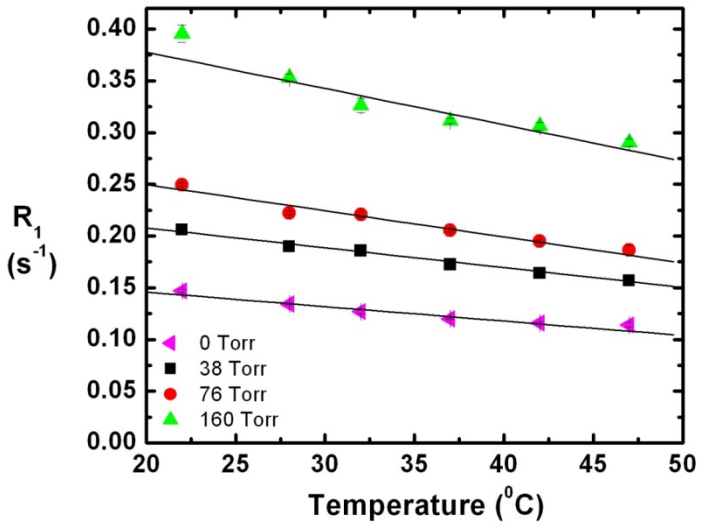

Figure 2.11: 5% v/v HS-15, 40% v/v HMDSO, 55% v/v DI-H_2O R_1 dependence on temperature at 4.7 T.

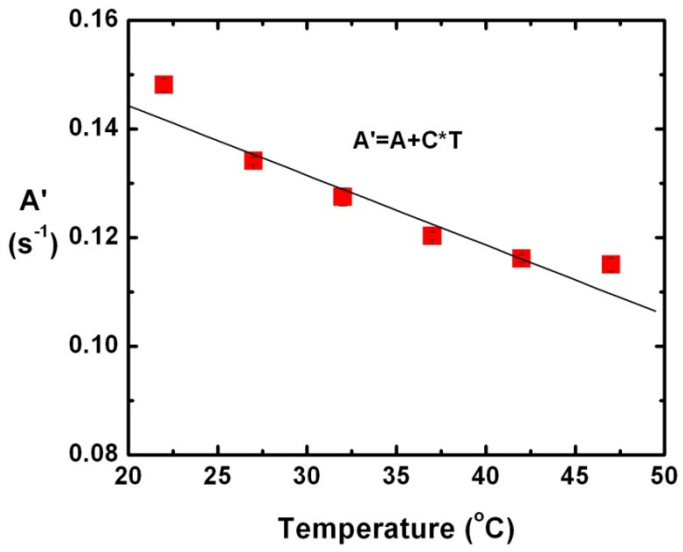

(a)

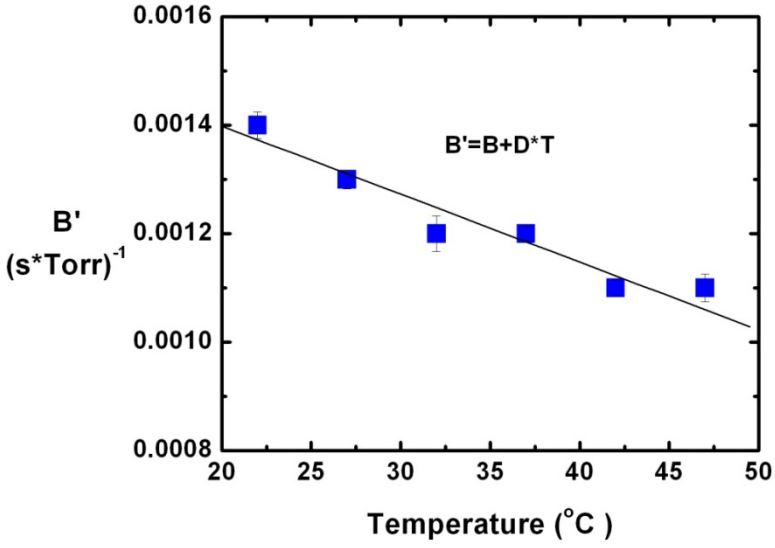

(b)

Figure 2.12: 5% v/v HS-15, 40% v/v HMDSO, 55% v/v DI-H_2O temperature dependence of constant (a) A' and (b) B' for at 4.7 T. Fitting data to a linear model resulted in calibration constants (a) A= 0.1699±0.0016 s^{-1}, C= -0.0013±4.53x10^{-5} (s*℃) $^{-1}$, (b) B= 0.0016±4.53x10^{-5} (s*Torr)$^{-1}$ and D = -1.25x10^{-5}±1.008x10^{-6} (s*Torr*℃) $^{-1}$.

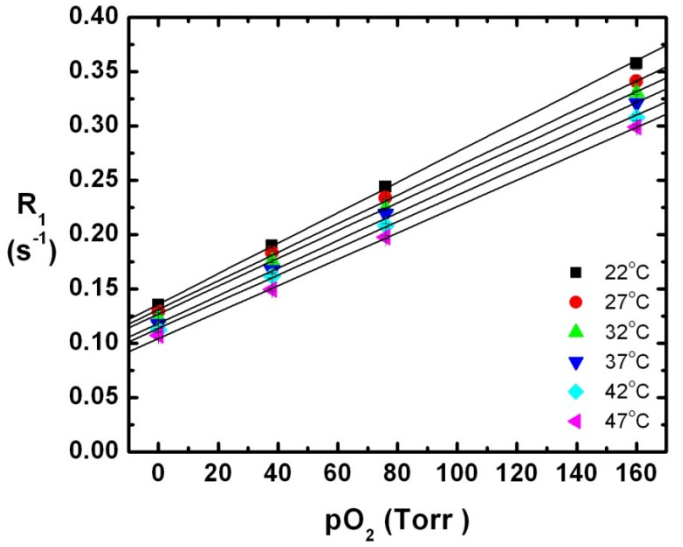

(a)

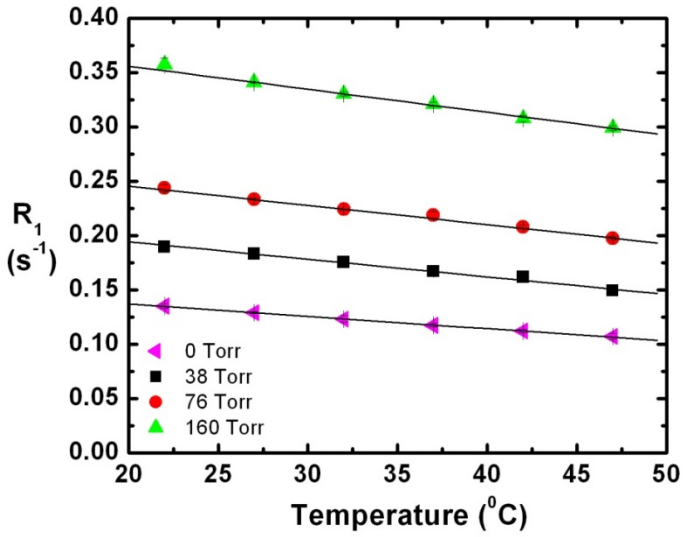

(b)

Figure 2.13: 5% v/v HS-15, 40% v/v HMDSO, 55% PBS (a) R_1 dependence on pO_2 at 4.7 T. (b) R_1 dependence on temperature at 4.7 T.

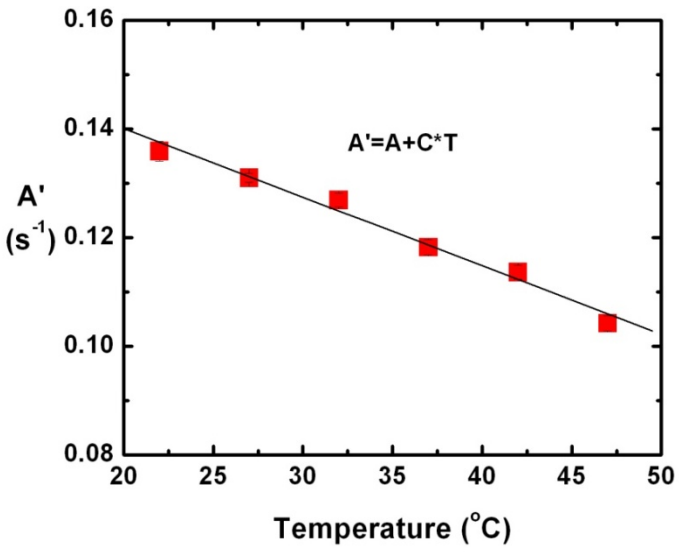

(a)

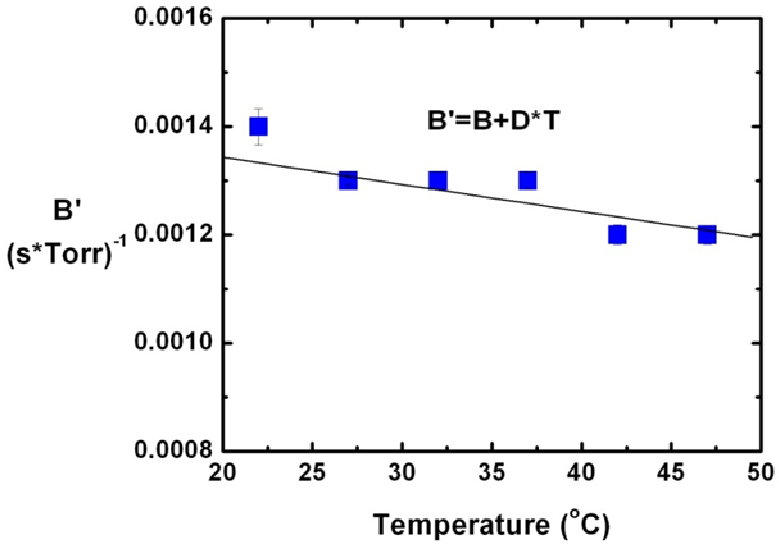

(b)

Figure 2.14: 5% v/v HS-15, 40% v/v HMDSO, 55% v/v PBS temperature dependence of constant (a) A' and (b) B' at 4.7 T. Fitting data to a linear model resulted in calibration constants (a) A= 0.1653 ± 0.0022 s^{-1}, C= -0.0013 ± 6.38x10^{-5} (s*℃) $^{-1}$, (b) B= 0.0014 ± 2.34x10^{-5} (s*Torr)$^{-1}$ and D= -5x10^{-6} ± 7.3x10^{-7} (s*Torr*℃) $^{-1}$.

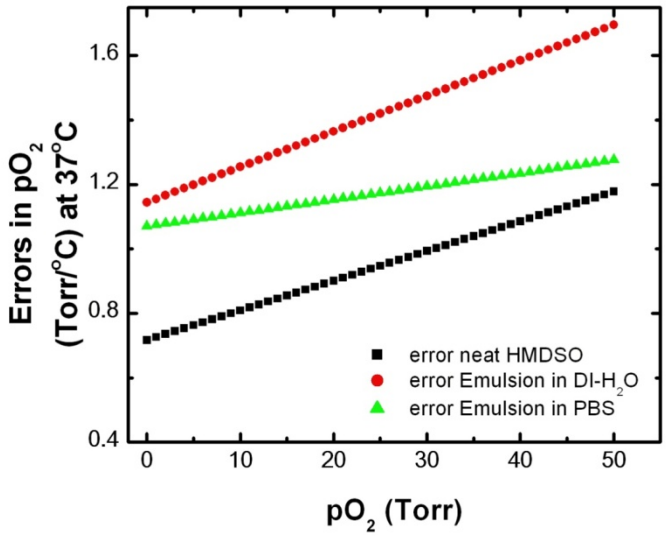

Figure 2.15: Comparison of simulated errors in pO_2 determination for emulsion in DI-H_2O and emulsion in PBS with neat HMDSO at 4.7 T.

2.3.4 Calibration of octamethyltrisiloxane (OMTSO) at 4.7 T and 9.4 T

OMTSO (Sigma Aldrich, St. Louis, MO, USA) is a symmetric molecule with a single NMR resonance close to that of tetramethylsilane (TMS). OMTSO has characteristics similar to that of HMDSO and its R_1 showed linear dependence on pO_2. Calibration of OMTSO was done at 4.7 T and 9.4 T using methods described earlier and characterization parameters were determined at both magnetic fields. At 4.7 T, A= 0.2295 ± 0.0021 s^{-1}, B=0.002 ± 4.1x10^{-5} $(s*Torr)^{-1}$, C=-0.002 ± 6.32x10^{-6} $(s*℃)^{-1}$, and D= -2.09x10^{-5} ± 1.2x10^{-6} $(s*Torr*℃)^{-1}$ error in pO_2 determination for 1℃ change in temperature was cal culated to be ~ 1.41 Torr/℃ for a pO_2 of 5 Torr. At 9.4 T A= 0.1985 ± 0.0015 s^{-1}, B= 0.0015 ± 6.2x$10^{-5}$$(s*Torr)^{-1}$, C= -0.0015 ± 5.3x$10^{-5}$ $(s*℃)^{-1}$ and D= -1.016x10^{-6} ± 2.05x$10^{-6}$$(s*Torr*℃)^{-1}$ with errors in pO_2 determination for 1℃ change in temperature at a pO_2 of 5 Torr being ~ 1.05 Torr/℃.

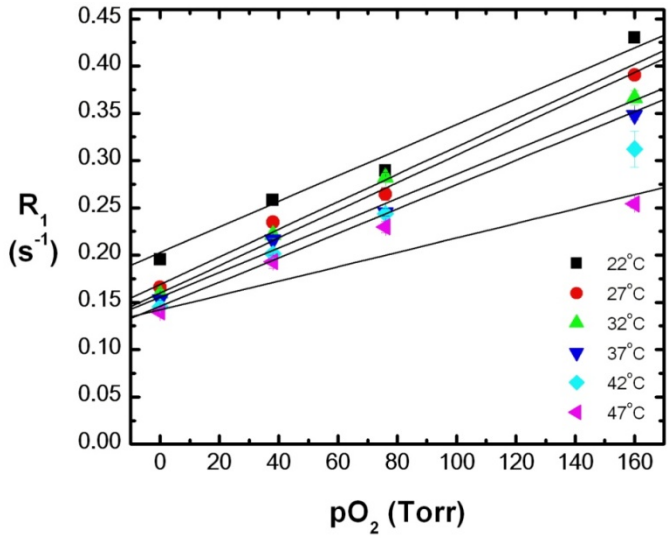

Figure 2.16: Neat OMTSO R_1 dependence on pO_2 on a 4.7 T scanner. Fitting data to a linear model resulted in calibration equation $R_1 = A' + B' * pO_2$.

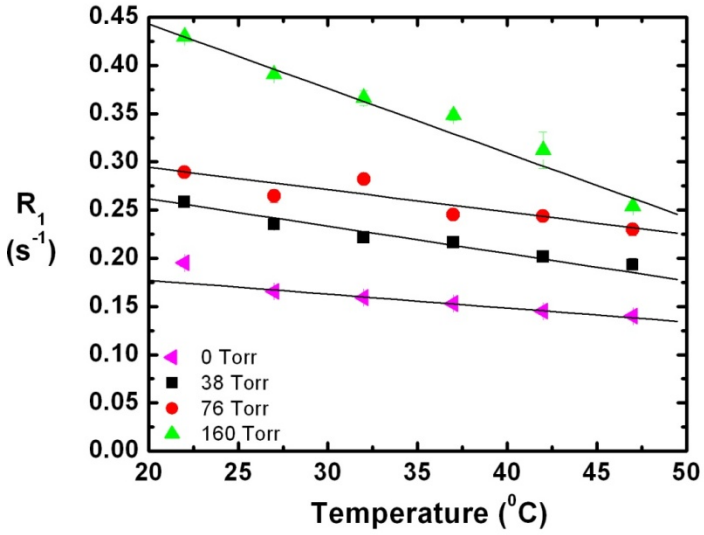

Figure 2.17: Neat OMTSO R_1 dependence on temperature at various pO_2 levels on a 4.7 T scanner.

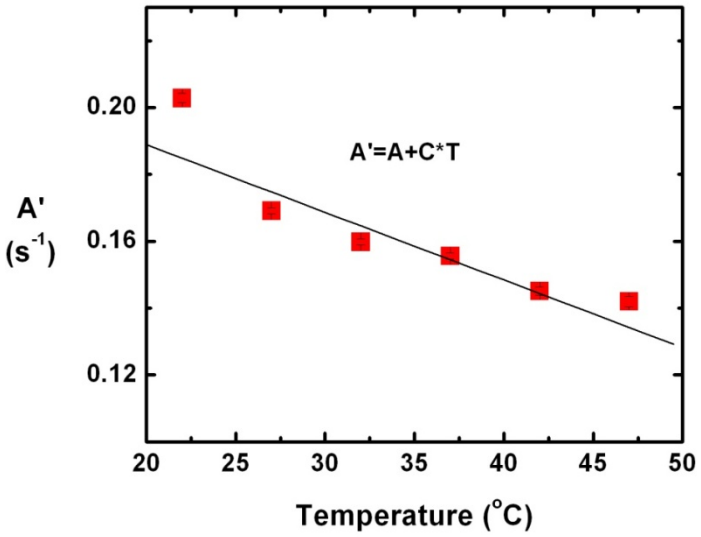

(a)

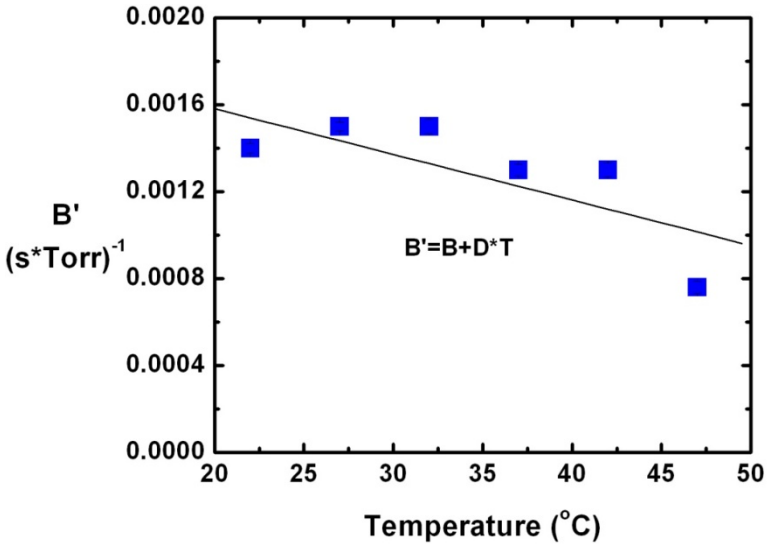

(b)

Figure 2.18: Neat OMTSO temperature dependence of constant (a) A' and (b) B' at 4.7 T. Fitting data to a linear model resulted in calibration constants (a) A= 0.2295 ± 0.0021 s-1, C=-0.002 ± 6.32x10^{-6} (s*℃) $^{-1}$, (b) B=0.002 ± 4.1x10^{-5} (s*Torr)$^{-1}$ and D= -2.09x10^{-5} ± 1.2x10^{-6} (s*Torr*℃) $^{-1}$.

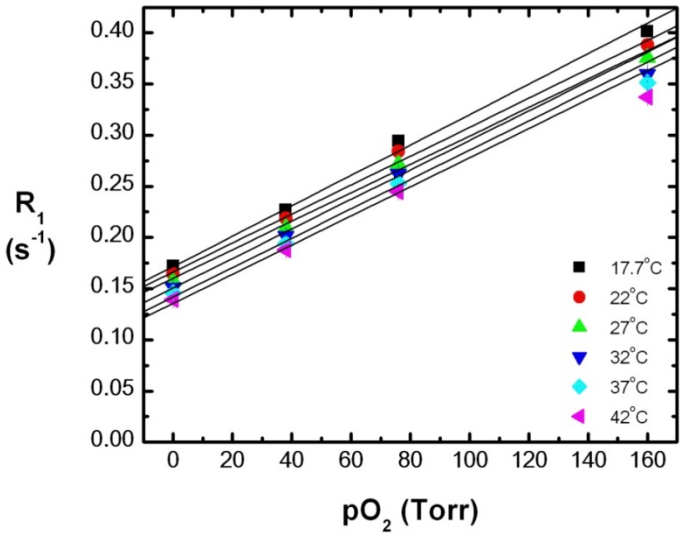

(a)

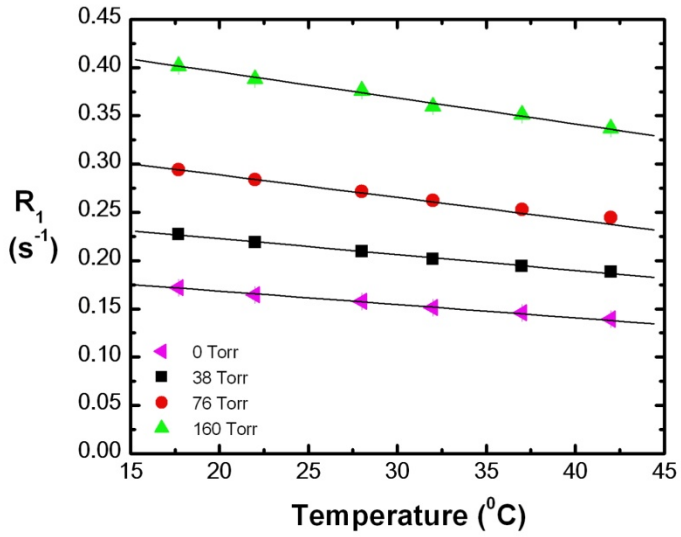

(b)

Figure 2.19: Neat OMTSO (a) R_1 dependence on pO_2 (b) R_1 dependence on temperature at 9.4 T scanner.

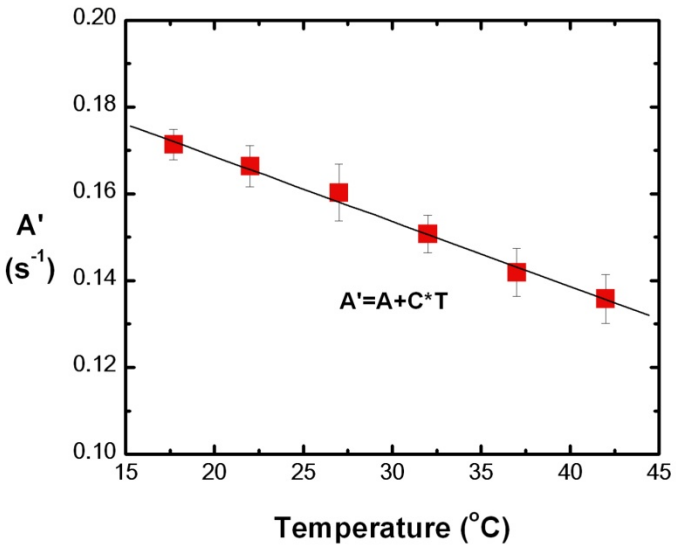

(a)

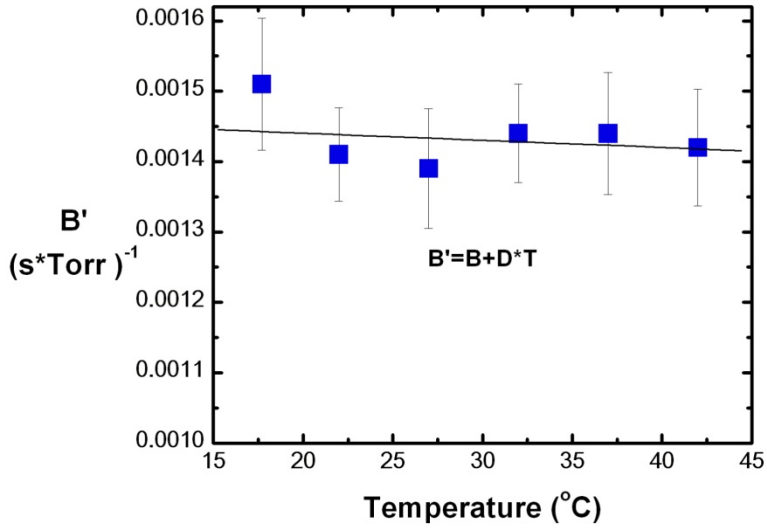

(b)

Figure 2.20: Neat OMTSO temperature dependence of constants (a) A' and (b) B' at 9.4 T. Fitting data to a linear model resulted in calibration constants (a) A= 0.1985 ± 0.0015 s^{-1}, C= -0.0015 ± 5.3x10^{-5} (s*℃) $^{-1}$, (b) B= 0.0015 ± 6.2x10^{-5} (s*Torr)$^{-1}$ and D= -1.016x10^{-6} ± 2.05x10^{-6} (s*Torr℃) $^{-1}$.

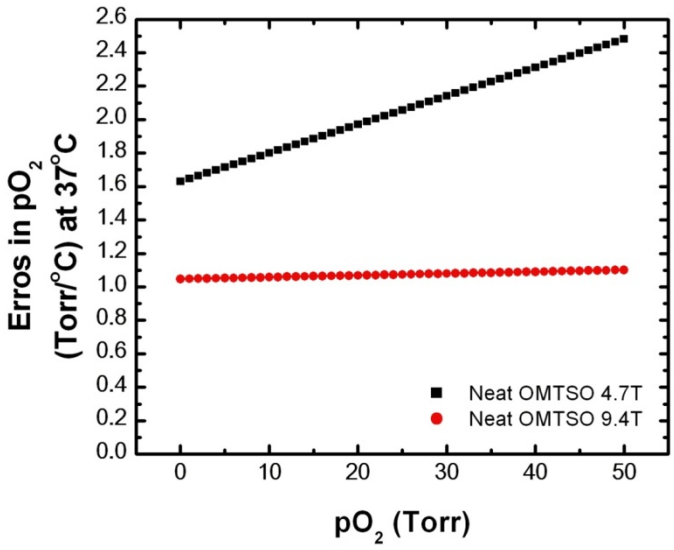

Figure 2.21: Comparison of simulated error in pO_2 determination for neat OMTSO with 1^{o}C change in temperature in hypoxia relevant pO_2 range at 37^{o}C on a 4.7 T and 9.4 T scanner.

CHAPTER 3

PULSES FOR QUANTITATIVE ^{1}H MR TISSUE OXIMETRY

3.1 Improving PISTOL

Proton Imaging of Siloxanes to map Tissue Oxygenation Levels (PISTOL) is a MR technique designed and implemented by my mentor Dr. Vikram D. Kodibagkar. Briefly, T_1 ($1/R_1$) values of probe and correspondingly the pO_2 were measured using a spin echo Echo Planar Imaging (EPI) based pulse sequence. It consists of an initial pulse burst saturation recovery preparation sequence followed by a variable time delay τ for magnetization recovery. After τ, probe frequency selective π/2 pulse is applied followed by a slice selective π pulse and EPI readout. Due to volume excitation by frequency selective π/2 pulse the technique limits the data acquisition to projections, hence multislice imaging is not possible. Also due to close proximity of probe and fat resonance there could be a possible contamination of probe signal by spurious fat signal leading to errors in quantification if the resonant frequency is not accurately centered on the HMDSO peak.

These issues can be addressed by the use of spatial spectral pulses (see section 1.4.3). As described in section 1.4.3, spatial spectral pulses are 2D RF pulses which are selective in space and spectral dimensions. These pulses were employed for selective excitation of probe resonance while suppressing water and fat resonances. By adding phase to the generated spatial spectral pulse it is possible to shift magnetization response in space thus making 3D oximtery possible.

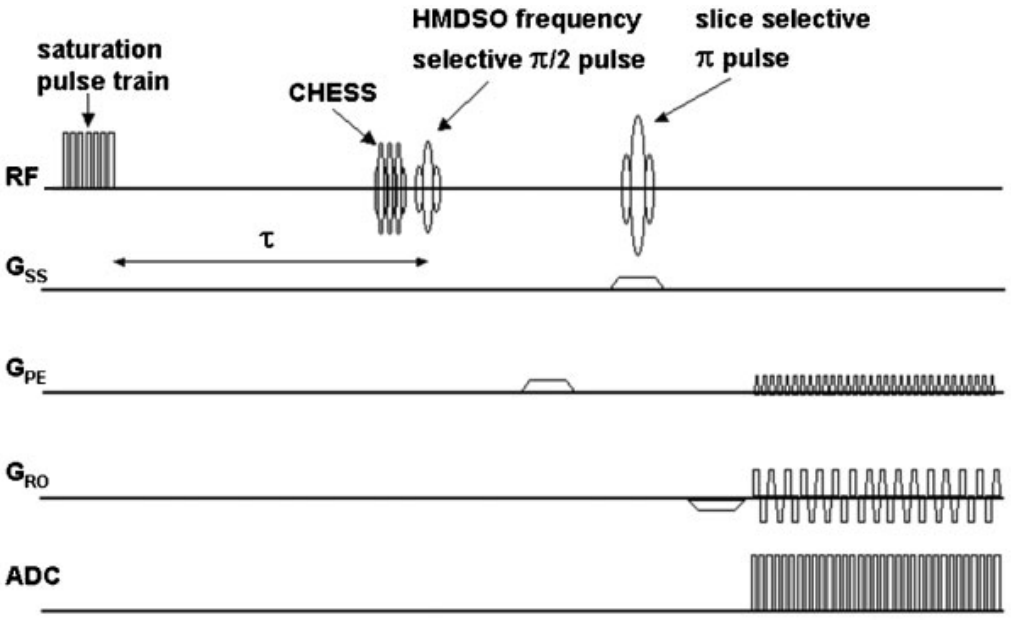

Figure 3.1: Pulse sequence for HMDSO relaxometry with optional CHESS fat and water suppression (PISTOL). (32)

3.2 Materials and Methods

3.2.1 Computer simulations

In order to understand the response of spatial spectral pulses computer simulations were carried out using MATLAB (The Mathworks Inc, MA). The object was assumed to be infinite and uniform, and relaxation effects were neglected. MATLAB based source code available at the Stanford website of Dr. John M. Pauly (41) was used to generate various excitation spatial spectral pulses using inverse SLR algorithm, and to calculate corresponding magnetization (M_{xy}) response using numerical solution of Bloch equations. An oscillating slice select gradient was designed in order to sample the $\mathbf{k}_{\omega}$ axis and to cover some region of spatial frequency space. Slice select gradient amplitude was determined using the following relation

$$G_z = \frac{\text{Bandwidth of subpulses}}{\gamma * \text{desired slice thickness}} \quad [18]$$

Gradient amplitudes of 7.28 G/cm (for TBW product of subpulses=4) and 14.56 G/cm (for TBW of subpulses=8) was required to obtain 3mm thick slices. Time for gradients to reach their maximum value or rise time was selected to be 100 μsec such that the slew rate was less than or equal to the maximum permissible slew rate for Varian Inova 9.4 T systems. RF subpulses were played throughout the entire duration of gradient lobe so as to obtain the thinnest possible slices. In order to effectively suppress signal from water and fat resonances and excite signal from probe frequencies various spatial spectral pulses were designed by varying pulse parameters such as, duration and time bandwidth product of subpulses which determines the position of desired and undesired components relative to the frequency side lobes and spatial slice profile respectively, the functional form of RF envelop (windowed sinc or minimum phase) which determines the **k** space weighting and thus the spatial and spectral slice profiles, duration of pulse which for a constant time bandwidth product determines the spectral bandwidth of excitation. The simulated pulses were scaled so that the sum of the amplitudes was equal to the desired tip angle in radians. A constant gradient in addition to slice select gradient was applied during excitation to simulate ω.

3.2.2 In vitro experiments

An *in vitro* phantom containing water, mineral oil (to simulate fat) and HMDSO in three separate microcentrifuge tubes (Fisher Scientific Inc.) arranged in the form of a triangle (see figure 3.2) was used. MR experiments were done on a 9.4 T Varian horizontal bore small animal scanner. Computer generated excitation spatial spectral pulses and corresponding oscillating slice select gradients were implemented in a spin echo pulse sequence consisting of π/2 spatial spectral pulse and a 4ms π pulse for refocusing. Images (matrix size:64x64, thickness=3mm, TR=1 sec, and minimum echo time) acquired using spatial spectral pulses were compared to a standard spin echo image for quantification of spectral selectivity using mean intensities of the selected ROI's. Magnetization responses of various pulses were compared by varying (1) duration and time bandwidth product of sub pulses, (2) pulse width and (3) spectral bandwidth.

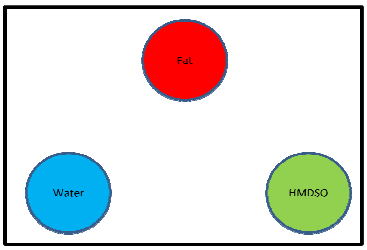

Figure 3.2: Initial design of *in vitro* phantom with fat, water and HMDSO in three separate tubes.

Improved phantom design: Initial design of the phantom had water, fat and HMDSO samples well separated from each other which would not be the case when imaging *in vivo*. Physiologically, *in vivo* imaging would involve water, fat and HMDSO molecules lying very close to each other. In order to simulate conditions that were more physiologically relevant a new phantom was used which consisted of three concentric tubes filled with water, mineral oil and HMDSO respectively (see figure 3.3). Computer generated spatial spectral pulses were implemented to a gradient echo sequence in addition to spin echo sequence as described previously. Images (matrix size:128x128 for spin echo images and 64x64(zero padded to128x128) for gradient echo images, thickness = 3mm, TR=1 sec, minimum echo time) acquired using spatial spectral pulses were compared to a standard spin echo, gradi
ent echo and chemical shift selective images for quantification of spectral selectivity using mean intensities of the selected ROI's.

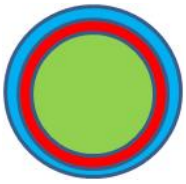

Figure 3.3: Improved *in vitro* phantom design with three concentric tubes. The outer most tube contains water, middle tube contains mineral oil and the inner most tube contains HMDSO.

3.2.3 In vivo experiments

A 20 ms, widowed sinc pulse, with sub lobe duration 0.43 ms and time bandwidth product =4 was seen to perform reasonably well for selective excitation of HMDSO *in vitro* and

was used for *in vivo* experiments. 50 µl of neat HMDSO was injected into the left thigh of an athymic nude mouse. Mean intensities of the image acquired using the above mentioned spatial spectral pulses (spin echo based sequence) were compared to mean intensity of the image obtained from chemical shift selective spin echo pulse sequence. Chemical shift selective spin echo pulse sequence consisted of a π/2 frequency selective pulse (on resonance for HMDSO) and slice selective π pulse for refocusing.

3.3 Results

3.3.1 Simulation results

Effect of time bandwidth product of subpulses: Spatial spectral pulses of 10 ms duration and sublobe duration of 0.43 ms were generated by varying functional form of the RF envelop (windowed sinc and minimum phase) and by varying time bandwidth product of the sub pulses (TBW=4, 8) with spectral pass band of RF envelope being ±250 Hz. Corresponding spatial profiles for slice thickness of 3mm at z=0 and ω=0 were simulated, it was observed that the slice profiles for pulses with time bandwidth product of subpulses = 8 was flat which is in accordance with theory since higher time bandwidth means greater number of lobes in the RF pulse which leads to better approximation of Fourier transform.

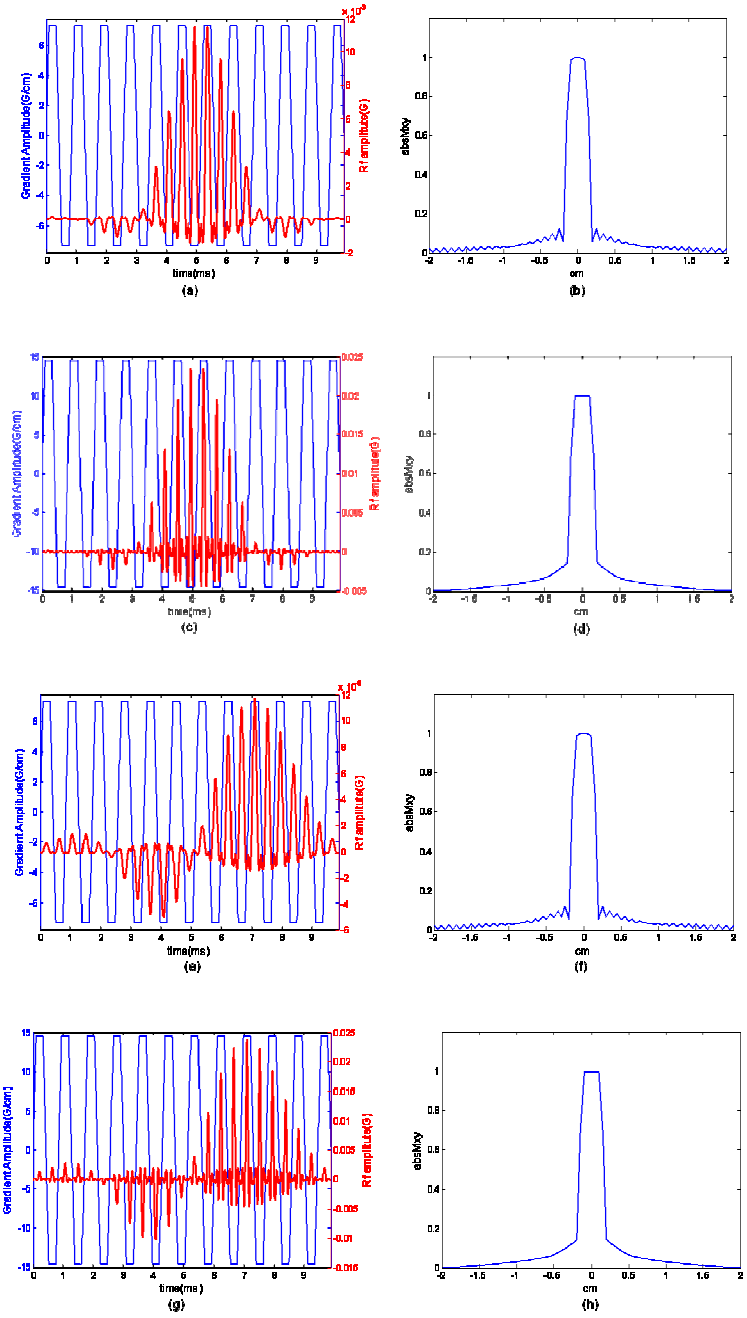

Figure 3.4: Effect of TBW of subpulses on spatial profiles. A 10 ms spatial spectral pulse with spectral pass band of ±250 Hz of type (a) wndowed sinc, time bandwidth of subpulses =4, (c) wndowed sinc, time bandwidth of subpulses =8, (e) minimum phase, time bandwidth of subpulses =4, (g) minimum phase, time bandwidth of subpulses =8 with corresponding slice profiles (b-h).

Effect of pulse duration:

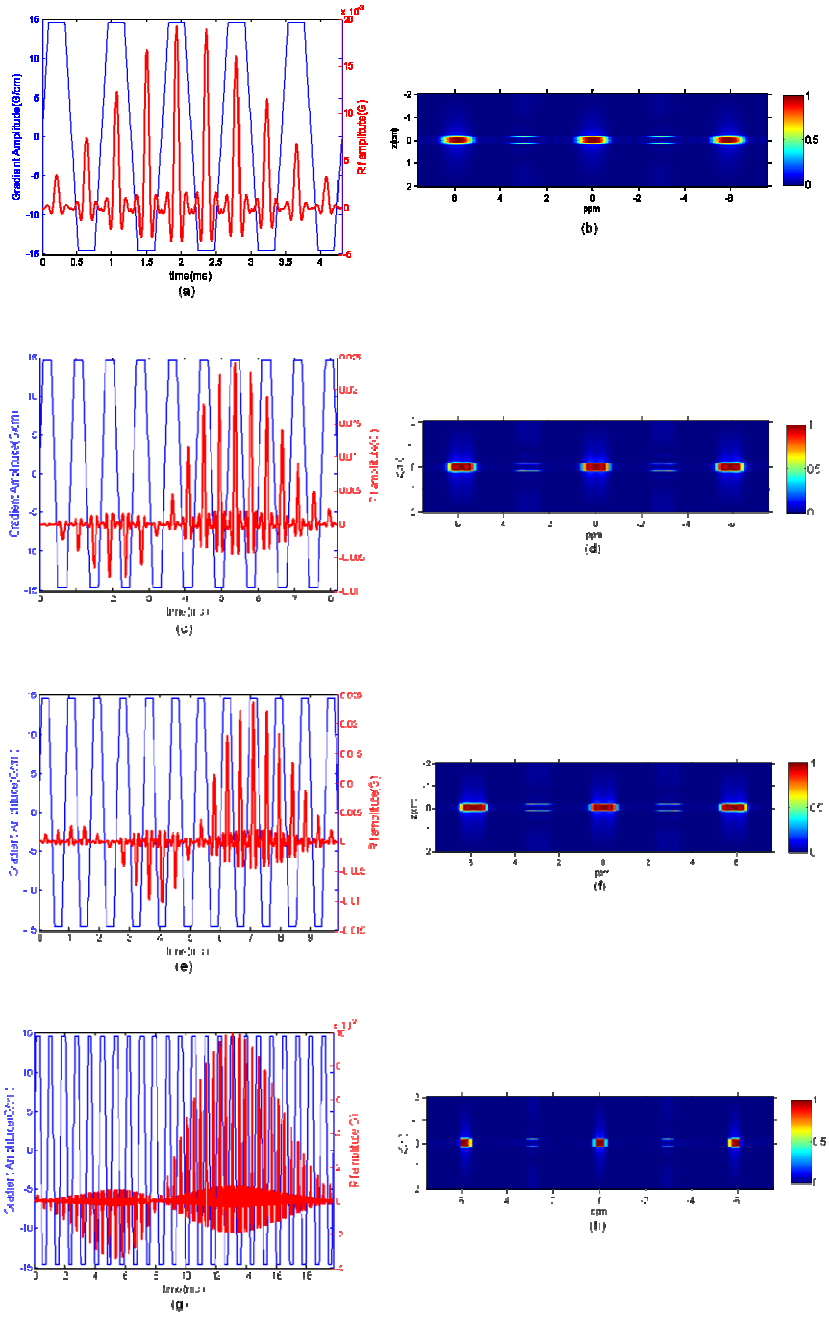

Figure 3.5: Effect of pulse duration on magnetization response. (a) 4 ms, (c) 8 ms, (e) 10 ms, (g) 20 ms duration spatial spectral pulses with RF envelop of the type minimum phase sinc and spectral pass band of ±250 Hz (4 ms, 8 ms, 10 ms) and ±100 (20 ms) and time bandwidth of subpulses being 8 have been generated (b-h) represent the corresponding magnetization response.

Effect of sub lobe duration: Spatial spectral pulses with varying sub pulses duration (0.71, 0.5, 0.43 ms) were generated to study their effect on magnetization response. As expected a 0.71 ms pulse resulted in even lobes repeating ±3.5*N ppm and odd lobes halfway between the even lobes (figure 3.12), 0.5 ms pulse resulted in even lobes repeating ±5*N ppm with odd lobes halfway between the even lobes (figure 3.13), 0.43 ms pulse resulted in even lobes repeating ±5.75*N ppm with odd lobes halfway between the even lobes (figure 3.14), (Where N=0, 1, 2, 3, 4…..).

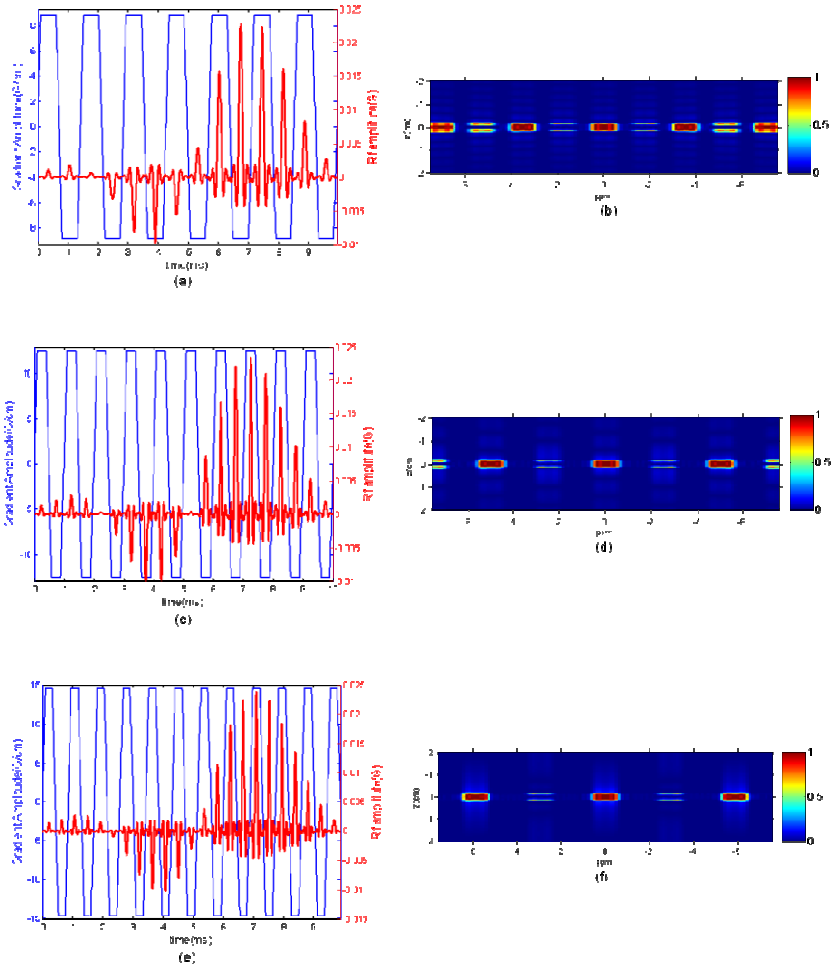

Figure 3.6: Effect of sub-lobe duration on magnetization response. A 10 ms pulse with RF envelop of type minimum phase and TBW of subpulses = 8 with sub lobe duration of (a) 0.71 ms, (c) 0.5 ms, (e) 0.43 ms and corresponding magnetization response (b-f).

3.3.2 In vitro experiments results

Mean intensity of water, fat and HMDSO reported by standard spin echo image was $(0.09 \pm 0.08)x10^{-3}$, $(2.75 \pm 2)x10^{-3}$, $(1.5 \pm 1.4)x10^{-3}$ respectively.

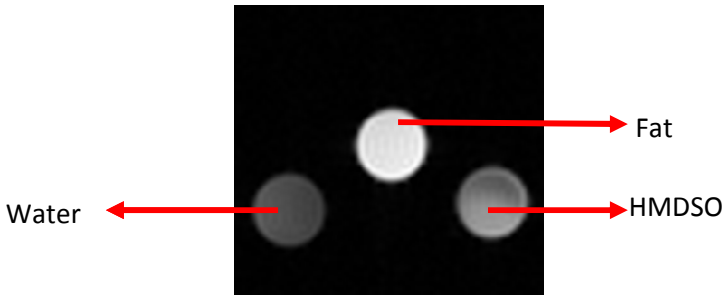

Figure 3.7: A standard 64x64 spin echo image of thickness 3mm with 4ms sinc π/2 and π pulse.

Effect of time bandwidth product: Effect of time bandwidth product of subpulses can be seen in Figure 3.16. It was observed that the response of spatial spectral pulse of duration 10 ms with RF envelop of type minimum phase and time bandwidth product of subpulses being 8 (see figure 3.16d) resulted in slice with uniform distribution of intensities. Figure 3.17 shows the mean of intensities of selected ROI's for images shown in Figure 3.16 reporting effect of time bandwidth product of subpulses on spectral selectivity.

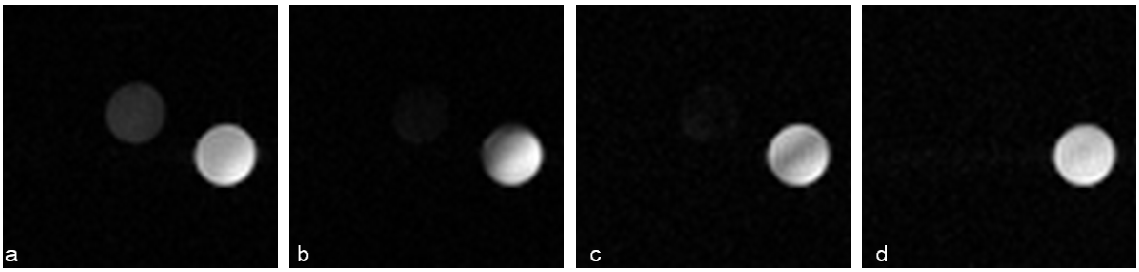

Figure 3.8: Effect of TBW of sub pulses on magnetization response and spectral selectivity (*in vitro*). Images acquired using pulse of 10 ms duration of type (a) windowed sinc, TBW product of subpulse=4, (b) windowed sinc, TBW product of subpulses=8, (c) minimum phase, TBW product of subpulses=4, (d) minimum phase, TBW of subpulses=8.

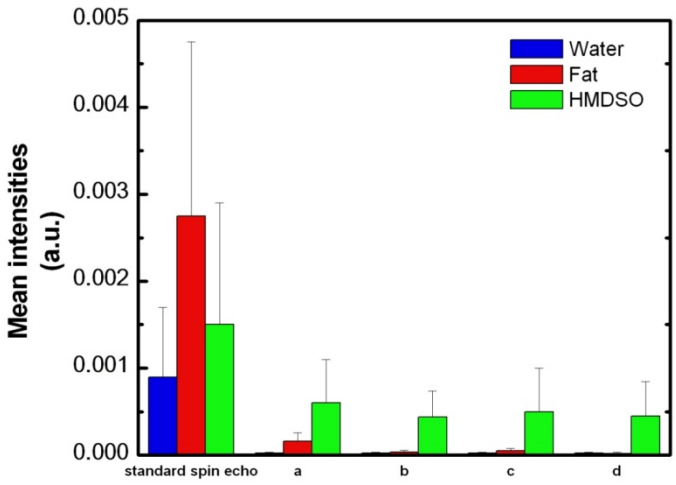

Figure 3.9: Comparison of mean intensities of selected ROI's for images acquired using various spatial spectral pulses. Duration of pulse = 10 ms of type (a) windowed sinc, TBW of subpulses=4, (b) windowed sinc, TBW of subpulses=8, (c) minimum phase, TBW of subpulses=4, (d) minimum phase, TBW of subpulses=8.

Effect of Pulse width: Figure 3.10 provides a qualitative assessment of effect of pulse width on magnetization response and spectral selectivity. It was seen that a pulse of duration 10 ms with RF envelop of the type minimum phase and time bandwidth of the subpulses being 8 resulted in uniform magnetization response (see figure 3.10c) and better spectral selectivity when compared to pulses with durations of 4, 8 and 10 ms (Figure 3.11).

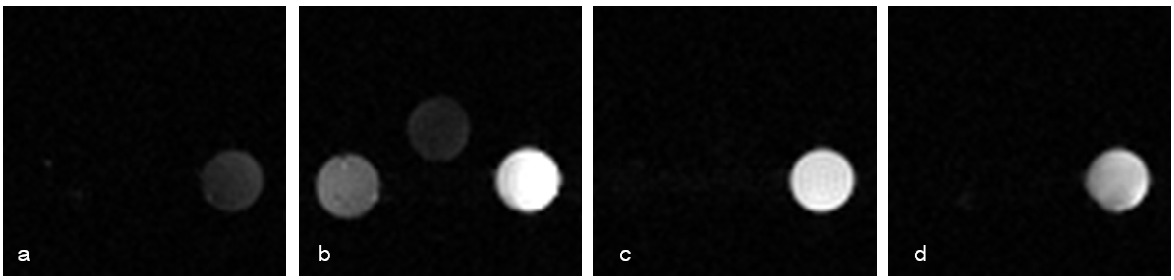

Figure 3.10: Effect of pulse width on magnetization response and spectral selectivity (*in vitro*). Images acquired using pulse of type minimum phase and TBW=8 with pulse width (a) 4ms, (b) 8ms, (c) 10ms, (d) 20ms.

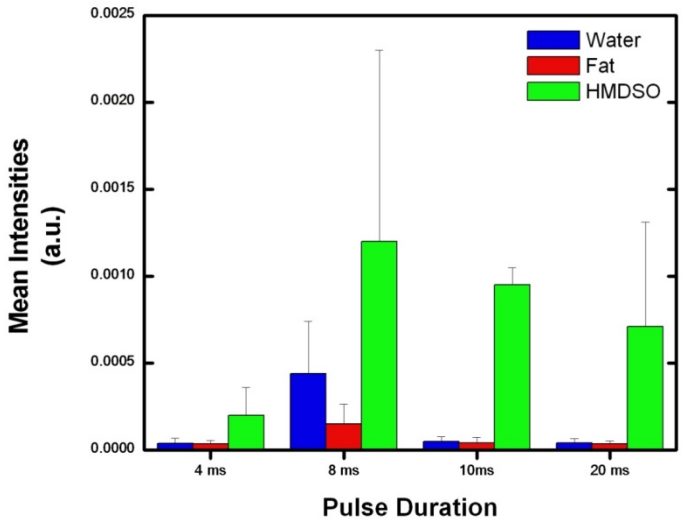

Figure 3.11: Mean intensities of selected ROI's for pulses of various durations with RF envelop of type minimum phase and TBW of subpulses=8.

Effect of duration of subpulses: Since duration of sublobe determines the spectral content that gets excited by the spatial spectral pulse. Effect of duration of subpulses on magnetization response was studied *in vitro*. It was seen that for a 10 ms pulse with RF envelop of type minimum phase, time bandwidth product of subpulses being 8 and spectral pass band being ±250 Hz, pulse with duration of sub lobe 0.71 ms excited water and fat resonances along with HMDSO resonance (see figure 3.12a) whereas pulses with sublobe duration of 0.5 ms and 0.43 ms provided better spectral selectivity for HMDSO resonance (see figure 3.12b and 3.12c).

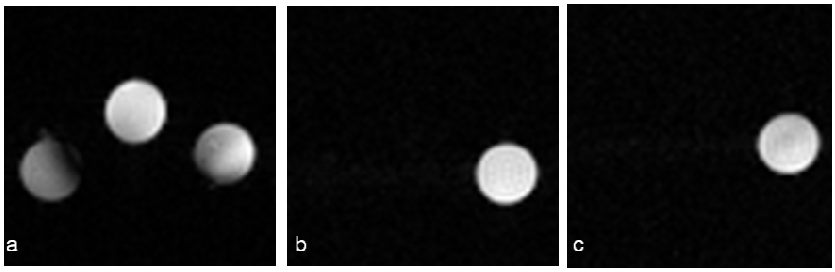

Figure 3.12: Effect of duration of sub pulses on magnetization response and spectral selectivity (*in vitro*). Images acquired using pulse of 10 ms duration of type minimum phase with sub pulses of duration (a) 0.71 ms, (b) 0.5 ms, (c) 0.43 ms.

3.3.3 In vitro experiments results (with improved phantom design)

As discussed previously a new phantom was designed to better reflect *in vivo* conditions. Magnetization response of pulses with varying pulse duration, functional form of RF envelop, time bandwidth product of subpulses was studied. For spin echo based experiments it was seen that a 20 ms pulse of RF envelop type windowed sinc, time bandwidth product of subpulses being 4, and spectral pass band of ±100 Hz provided better suppression of water and fat resonances when compared to standard spin echo images and chemical shift selective (on resonance for HMDSO) images with some loss in HMDSO signal. Similar results were obtained when spatial spectral pulses were implemented in gradient echo based pulse sequence (see figure 3.15).

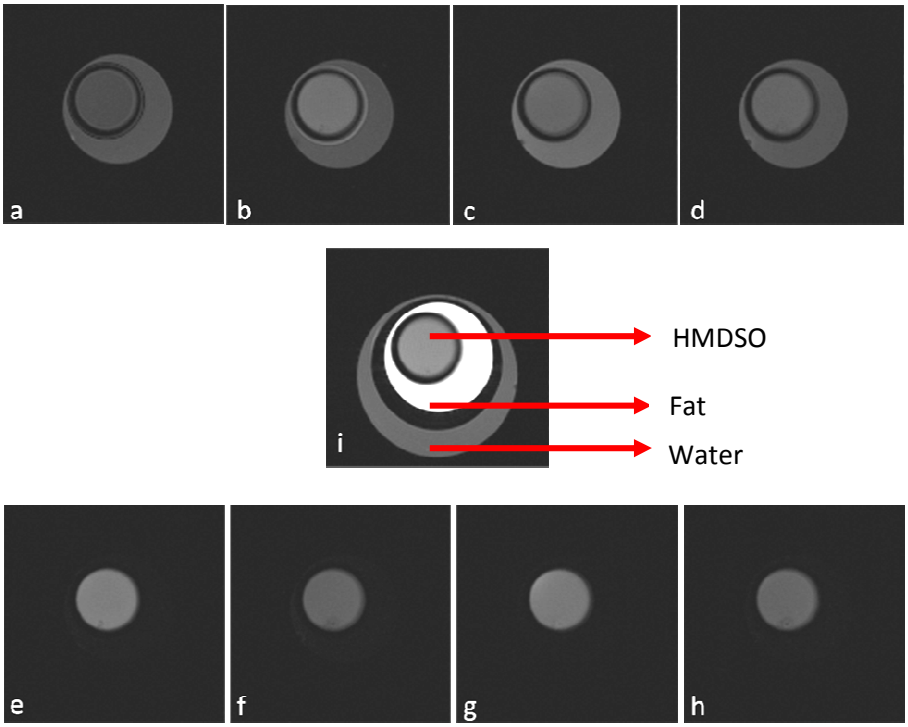

Figure 3.13: Response of spatial spectral pulses implemented in a spin echo based pulse sequence with improved phantom design. A 4ms (top row) and 20 ms (bottom row) pulse with sublobe duration of 0.43 ms of type (a,e) windowed sinc, with TBW of subpulses=4, (b,f) windowed sinc, with TBW of subpulses=8, (c,g) minimum phase, with TBW of sub pulses=4, (d,h) minimum phase with TBW of subpulses=8 compared with (i)standard spin echo image (center row).

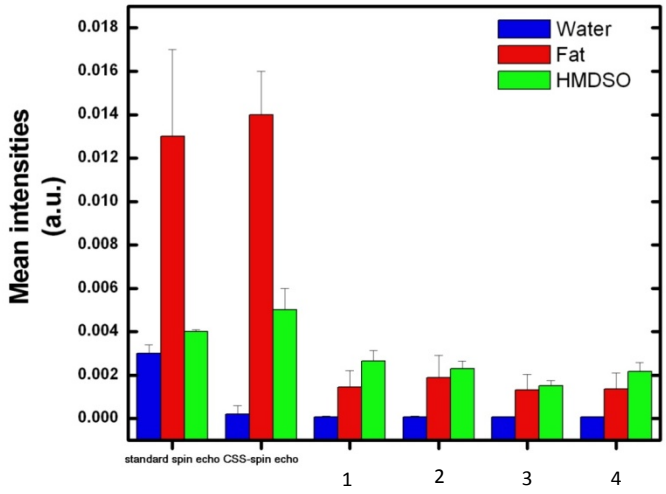

(a)

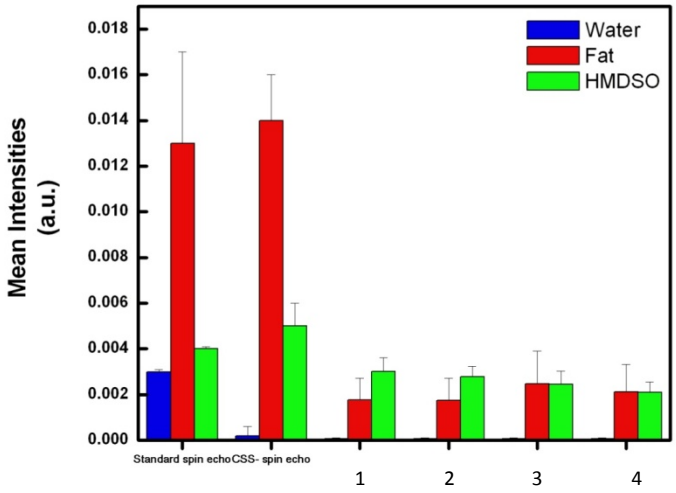

(b)

Figure 3.14: Comparison of mean intensities of selected ROI's for images acquired using a spatial spectral pulse implemented in a spin echo pulse sequence of duration (a) 4 ms and (b) 8 ms. Pulses of type (1) windowed sinc, TBW product of subpulses=4, (2) minimum phase, TBW product of subpulses=4, (3) windowed sinc, TBW product of subpulses=8, (4) minimum phase, TBW product of subpulses=8.

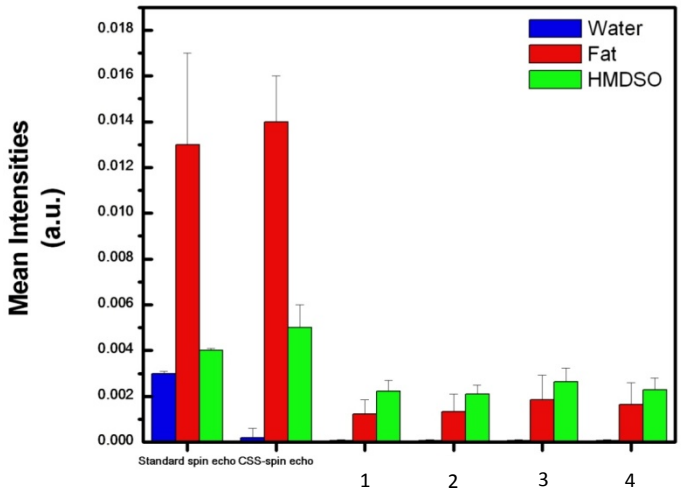

(a)

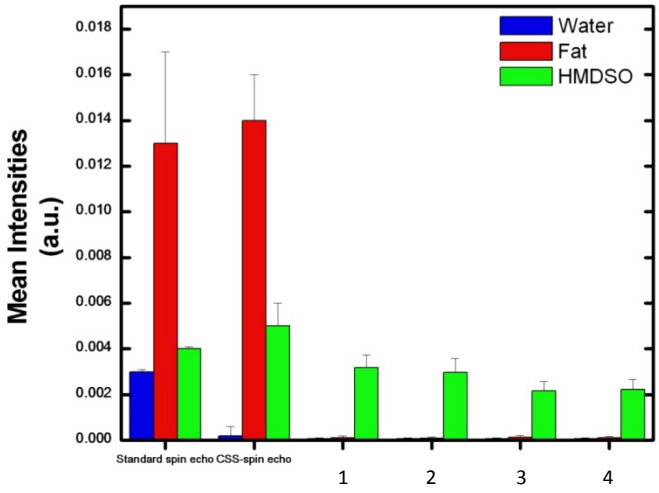

(b)

Figure 3.15: Comparison of mean intensities of selected ROI's for images acquired using a spatial spectral pulse implemented in a spin echo pulse sequence of duration (a) 10 ms and (b) 20 ms. Pulses of type (1) windowed sinc, TBW product of subpulses=4, (2) minimum phase, TBW product of subpulses=4, (3) windowed sinc, TBW product of subpulses=8, (4) minimum phase, TBW product of subpulses=8.

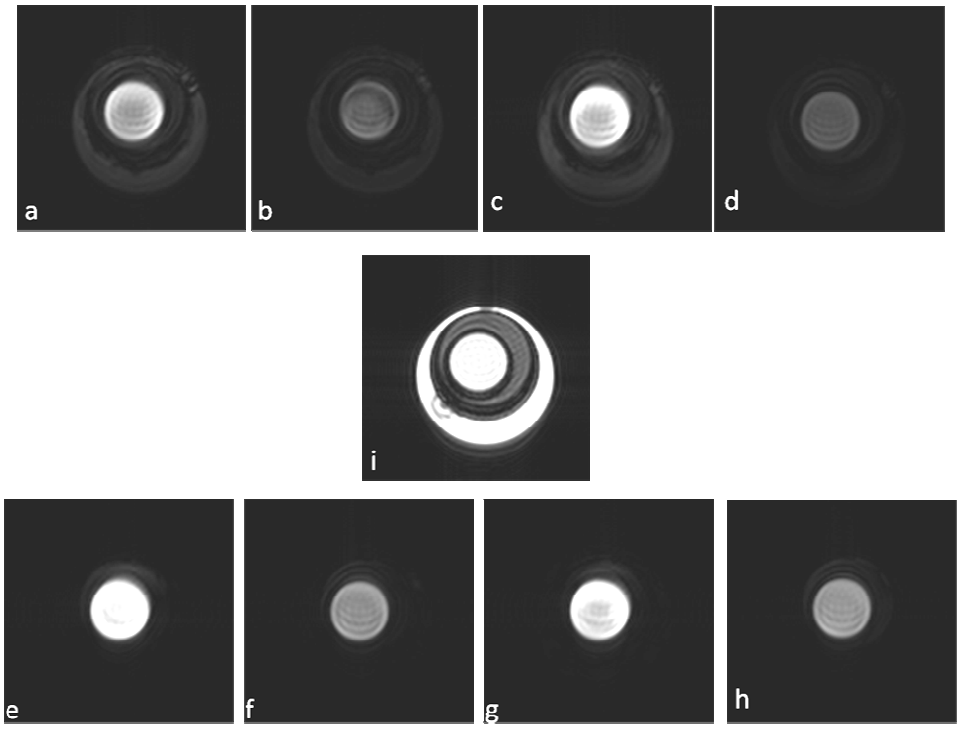

Figure 3.16: Response of spatial spectral pulse implemented in a gradient echo based pulse sequence with improved phantom design. A 4 ms (top row) and 20 ms (bottom row) pulse implemented in a gradient echo based pulse sequence of type (a,e) windowed sinc, with TBW of subpulses=4, (b,f) windowed sinc, with TBW of subpulses=8, (c,g) minimum phase, with TBW of sub pulses=4, (d,h) minimum phase with TBW of subpulses=8 compared with (i) standard gradient echo image (center row).

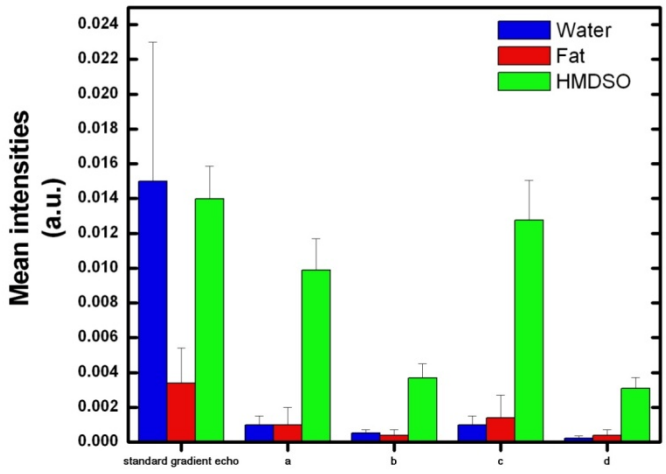

(a)

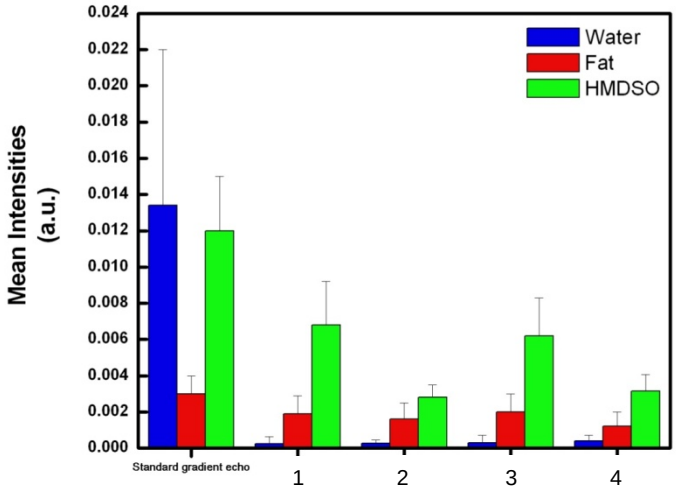

(b)

Figure 3.17: Comparison of mean intensities of selected ROI's for images acquired using a spatial spectral pulse implemented in a gradient echo pulse sequence of duration (a) 4 ms and (b) 8 ms. Pulses of type (1) windowed sinc, TBW product of subpulses=4, (2) windowed sinc, TBW product of subpulses=8, (3) minimum phase, TBW product of subpulses=4, (4) minimum phase, TBW product of subpulses=8.

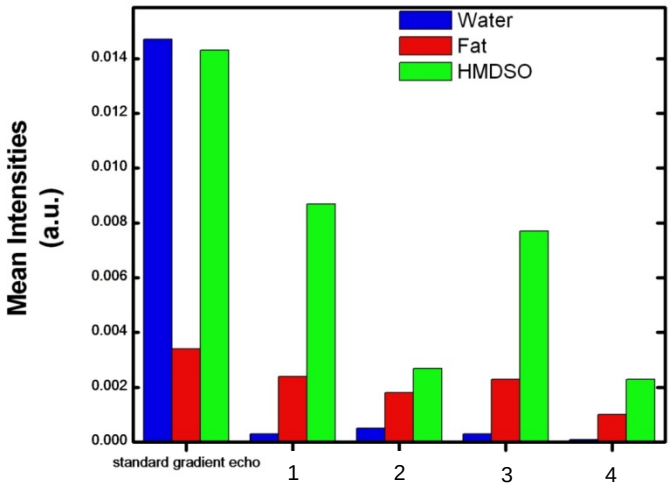

(a)

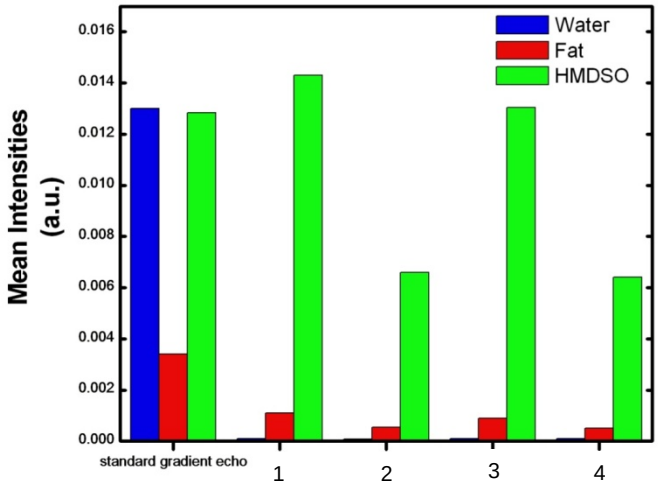

(b)

Figure 3.18: Comparison of mean intensities of selected ROI's for images acquired using a spatial spectral pulse implemented in a gradient echo pulse sequence of duration (a) 10 ms and (b) 20 ms. Pulses of type (1) windowed sinc, TBW product of subpulses=4, (2) windowed sinc, TBW product of subpulses=8, (3) minimum phase, TBW product of subpulses=4, (4) minimum phase, TBW product of subpulses=8.

3.3.4 In vivo experiment results

Spatial spectral pulses implemented in spin echo based pulsed sequence were employed for *in vivo* studies by the methods described previously. It was observed that there was excellent suppression of water and fat signal by spatial spectral pulse when compared qualitatively to chemical shift selective spin echo image. By varying repetition time (TR) a T_1 map was obtained for the image obtained in (c). Mean T_1 of 4.2 s and corresponding mean thigh pO_2 of 118 Torr was reported. Although spatial spectral pulse demonstrated excellent spectral selectivity it was also observed that there was decrease in detected HMDSO signal by spatial spectral pulses when compared to chemical shift selective image.

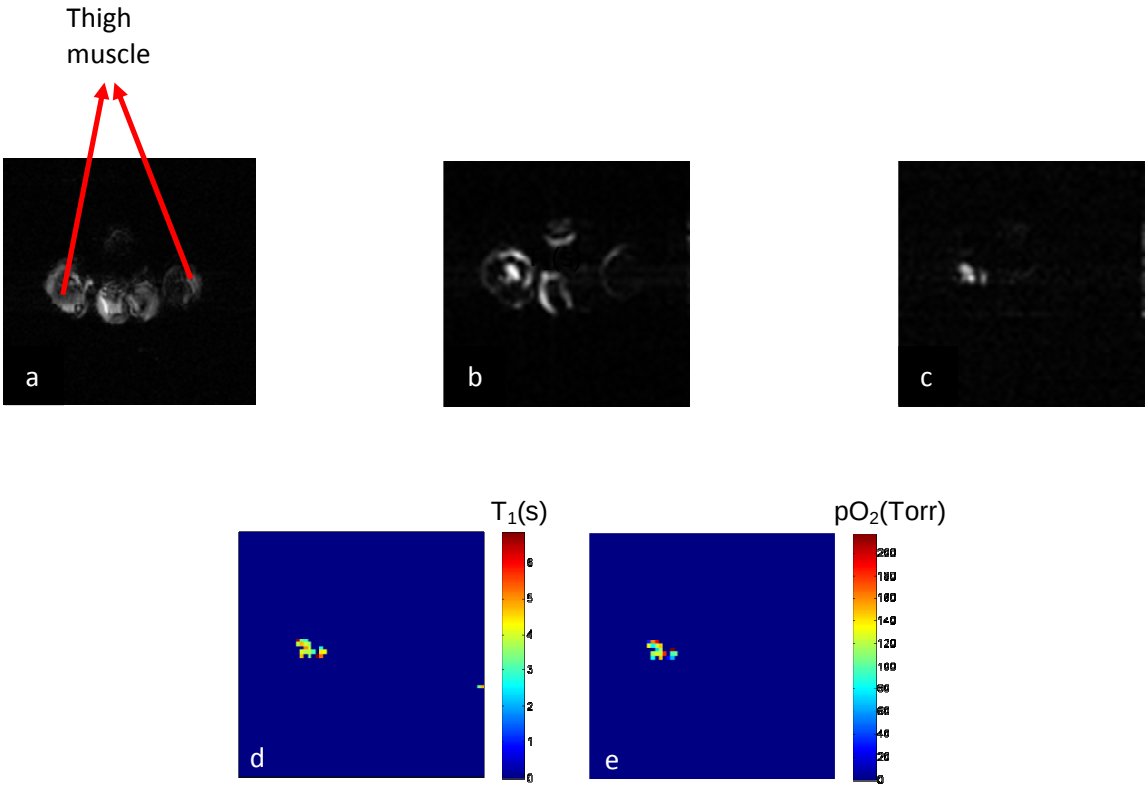

Figure 3.19: *In vivo* testing of spatial spectral pulse. 50 µl of neat HMDSO was injected into the left thigh of the animal and (a) scout image was obtained.(b) corresponding chemical shift selective image was obtained (on resonance HMDSO), (c) image obtained using a 20 ms spatial spectral pulse with RF envelop of type windowed sinc and TBW product of subpulses=4 implemented in a spin echo based sequence . Image (c) shows improvement in fat suppression when compared to (b).(d) T_1 map for the image obtained in (c) and corresponding pO_2 map (e).

CHAPTER 4

CONCLUSION AND DISCUSSION

This study demonstrated the potential of HMDSO, HMDSO based nano emulsions and OMTSO as promising pO_2 probes for ^1H MR oximetry. Excellent suppression of water and fat to aid selective imaging of such pO_2 probes was accomplished using spatial spectral pulses.

Calibration data acquired by me and calibration data acquired previously by my mentor Dr. Kodibagkar(38) were compared. From the calibration equations (refer section 2.3.1) it was noted that for a pO_2 5 Torr difference in T_1 calculated from my calibration equation and T_1 calculated from previous calibration equation is 0.11 (error ~ 1%) seconds (using the full calibration point) and 0.27(error ~ 3%) seconds (without 760 Torr point). Also for a T_1 of 8.5 seconds difference in pO_2 obtained from the calibration equations were ~ 1.2 Torr (with full calibration point). Such low errors suggest high reproducibility of the technique and calibration.

Calibration of neat HMDSO to demonstrate dependence of its longitudinal relaxation rate R_1 on temperature and pO_2 at 4.7 T has been previously and reported (38). To understand the effect of magnetic field strength calibration of neat HMDSO with respect to changes in $pO_2$and temperature was performed on a 9.4 T scanner. Measuring tissue oxygenation using HMDSO at 9.4 T has following advantages 1) species have larger chemical shift separation between them which aids in selective excitation, 2) increase in net magnetization ($M_0 \propto B_0$). It is well known at higher magnetic fields the relaxation time gets longer thus increasing the total imaging time. Our results suggest that for HMDSO at 9.4 T, T_1 at 37℃ ranged from 9 seconds (pO_2=0 Torr) to 3.21seconds (pO_2=160 Torr) which differed by ~ 3.5% from T_1 obtained at 4.7 T indicating no substantial increase in imaging time. Also calculated error in pO_2 determination as given by Equation [17] at 37℃ for 1℃ change in te mperature was~ 1.2 Torr/℃ at 9.4 T and ~ 0.8 Torr/℃ at 4.7 T when actual pO_2 value was 5 Torr. Since imaging time at 9.4 T was

same as for 4.7 T with no significant increase of error in pO_2 determination, imaging of HMDSO would be desired on 9.4 T.

Various HMDSO based oil in water nanoemulsions have been synthesized successfully using PEGylated non ionic surfactant and have been characterized with respect to changes in pO_2 and temperature. As seen from Table 2.1 these nanoemulsions have oxygen sensitivity similar to neat HMDSO indicating potential of and being used as a pO_2 probe following systemic delivery. Temperature dependence of 5% v/v HS-15, 40% v/v HMDSO, 55% v/v DI-H_2O and 5% v/v HS-15, 40% v/v HMDSO, 55% v/v PBS was seen similar to that of neat HMDSO (38). Error in pO_2 determination was calculated at a temperature of 37℃ for changes in temperature by 1℃ at an actual pO_2 of 5 Torr and was found to be ~1.2 Torr/℃ for 5% v/v HS-15, 40% v/v HMDSO, 55% v/v DI-H_2O, ~ 1.1 Torr/℃ for 5% v/v HS-15, 40% v/v HMDSO, 55% v/v PBS, compared to 0.8 Torr/℃ for neat HMDSO.

Calibration of OMTSO with respect to changes in temperature and pO_2 was done at 4.7 T and 9.4 T scanner. It was observed that longitudinal relaxation rate of OMTSO varied linearly with respect to changes in pO_2.The results demonstrate potential of OMTSO for use as a pO_2 reporter molecule. At the resolution used here, a single resonance was observed for OMTSO. At a constant temperature of 37℃ OMTSO ($B'_{OMTSO@4.7\ T} = 0.0013 \pm 2.66x10^{-5}$, $B'_{OMTSO@9.4\ T} = 0.0014 \pm 8.66x10^{-5}$) had oxygen sensitivity similar to HMDSO ($B'_{HMDSO@4.7\ T} = 0.0013 \pm 5.5x10^{-5}$, $B'_{HMDSO@9.4\ T} = 0.0012 \pm 8.81x10^{-6}$). Another important observation was that OMTSO had higher anoxic relaxation rate (A') compared to neat HMDSO at 4.7 T and 9.4 T respectively. This characteristic of OMTSO can be further exploited to map tissue oxygenation faster than HMDSO. It should be also noted that boiling point of neat OMTSO (153℃) is higher than the boiling point of neat HMDSO (101℃) thus advantageo us for emulsification process (42). Errors in pO_2 determination for OMTSO were found to be ~1.4 Torr/℃ at 4.7 T and ~1.07 Torr/℃ at 9.4 T , compared to ~0.8 Torr/℃ at 4.7 T and ~1. 2 Torr/℃ at 9.4 T for HMDSO, at an actual

pO_2 of 5 Torr with change in temperature by 1℃ at 37℃. Thus, OMTSO is identified as a promising pO_2 probe which could enable faster mapping of tissue oxygenation than HMDSO.

In this study excellent suppression of water and fat resonances was demonstrated by using spatial spectral pulses *in vitro and in vivo*. Spatial spectral pulses have been successfully designed, generated, implemented and tested on a 9.4 T pre clinical Varian MR scanner. Computer simulations were helpful in understanding behavior of various pulses and all simulation results were consistent with theory. *In vitro* testing of computer generated spatial spectral pulses was done by implementing these pulses in a gradient echo and spin echo based pulse sequence. From my *in vitro* experiments it was observed that magnetization response of a particular pulse is shimming dependant. For initial phantom (see figure 3.3) a 10 ms minimum phase pulse with TBW=8 and spectral passband ±250 Hz provided 97% suppression of water and 99% suppression of fat signal.

When the phantom design was changed (see figure 3.4) a 20 ms windowed sinc pulse with TBW=4 and spectral passband of ±100 Hz provided 98% suppression of water signal with respect to water signal from standard spin echo and 66% suppression of water signal with respect to water signal from chemical shift selective sequence (on resonance for HMDSO) and 99% suppression of fat signal with respect to fat signal from standard spin echo and chemical shift selective sequence (on resonance for HMDSO). A 20 ms sec pulse was able to suppress water and fat signal for improved phantom design as it had a spectral passband of ±100 Hz as compared to spectral passband of ±250 Hz for 10 ms sec pulse. This could be better understood by looking at figure 4.1.

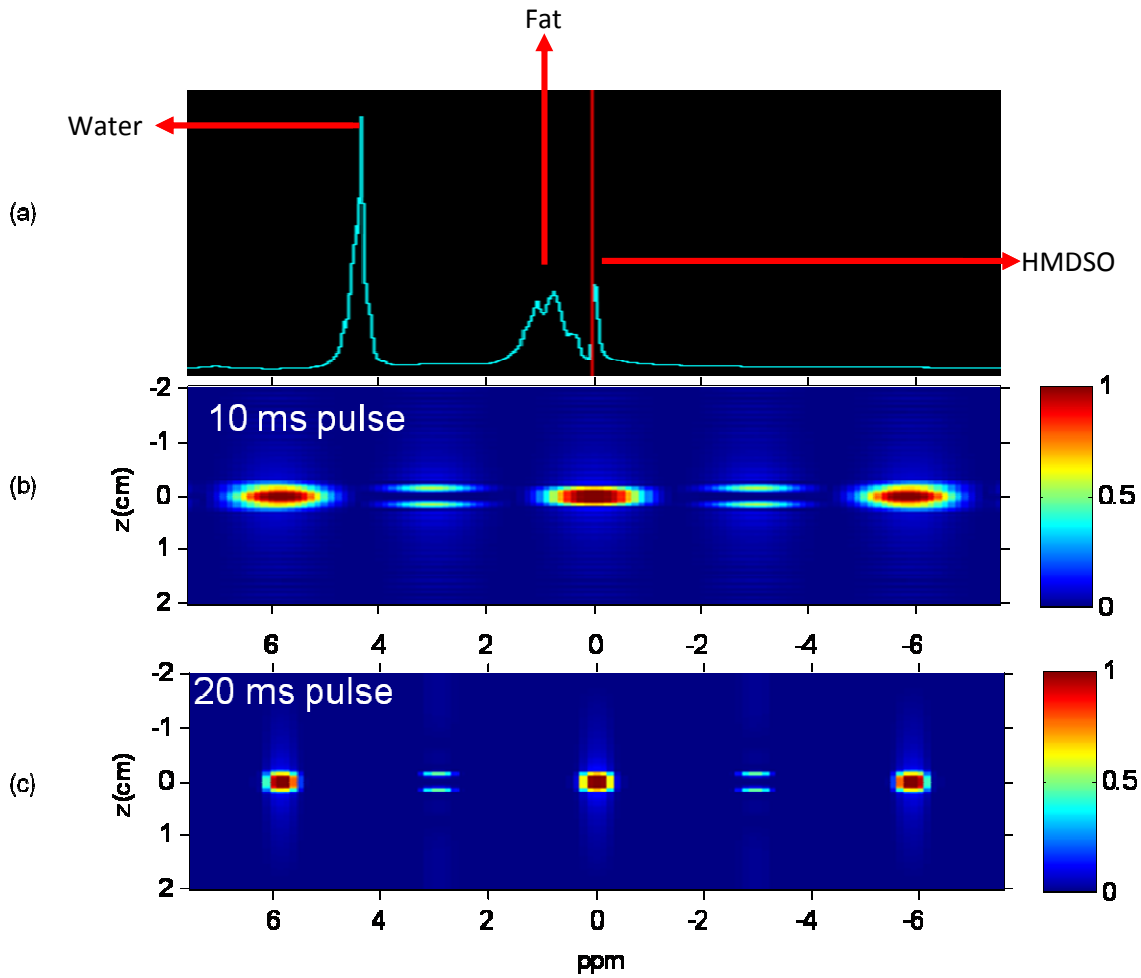

Figure 4.1: Effect of spectral passband on the magnetization response. (a) spectrum obtained for the phantom described in Figure 3.3. (b) Simulated magnetization response for a 10 ms sec pulse with spectral passband of ±250 Hz, (c) Simulated magnetization response for a 20 ms pulse with spectral passband of ±100 Hz.

Along with suppression of fat and water signal a corresponding decrease in detection of HMDSO signal was observed indicating that the technique is a low sensitivity technique. Spatial spectral pulses implemented in gradient echo based sequence resulted in 99% suppression of water signal and 67% decrease in fat signal when compared to water and fat signal from standard gradient echo sequence. *In vivo* experiment validated the excellent suppression of fat and water although there was some loss of HMDSO signal as well.

Future work involves implementation of these pulses into PISTOL sequence to further improve the accuracy and robustness of the technique.

APPENDIX A

PARTICLE SIZE DATA

Particle size determination

Table below summarizes various nanoemulsioins that were formulated, and reports the corresponding particle size for the emulsions. Particle sizes were measured by using methods described previously. Polydimethylsiloxane (PDMS) was bought from Sigma Aldrich, St. Louis, MO, USA.

Probe	**Mean Radius of Particle Size (nm)**
2% v/v PEG-PDMS (600), 40% v/v HMDSO, 58% v/v PBS	281.7
2% v/v PEG-PDMS (3000), 40% v/v HMDSO, 58% v/v PBS	264.6
2% v/v PEG-PDMS (600), 40% v/v PDMS, 58% v/v PBS	130.5
2% v/v PEG-PDMS (3000), 40% v/v PDMS, 58% v/v PBS	222.5
2% v/v PEG-PDMS (600), 40% v/v OMTSO, 58% v/v PBS	155.7
5% v/v PEG-PDMS (600), 40% v/v OMTSO, 55% v/v PBS	108.0
8% v/v PEG-PDMS (600), 40% v/v OMTSO, 52% v/v PBS	88.8
2% v/v PEG-PDMS (3000), 40% v/v OMTSO, 58% v/v PBS	319.2
5% v/v PEG-PDMS (3000), 40% v/v OMTSO, 55% v/v PBS	283.1
8% v/v PEG-PDMS (3000), 40% v/v OMTSO, 52% v/v PBS	340.9

.

APPENDIX B

MATLAB CODE FOR GENERATING SPATIAL SPECTRAL PULSES

```
clc
close all
clear all
warning off
Mxy=[];
%% simulation of oscilating gradients
% g1=[[0:1]/2 ones(1,4) [1:-1:0]/2];
%  g1=[[0.5:15.5]/16 ones(1,32) [15.5:-1:0.5]/16];
%  g1=[ ones(1,32)];
% g=0.94*g1;
% g=g1+1i*g2;
%% Calculation of duration of sub lobes
   % 9.4 T details
   % HMDSO at 0 Hz
   % Fat at around 528 Hz
   % Water at around 1880 Hz

   % T     This actually will determine which frequencies will be excited
   %       T=1/F ----> where F is the frequency where primary lobe occurs
   %       Secondary lobe occurs at F/2
   prim_freq=2.3;               %--frequency in Khz at which primary lobe should occur
   tgx=time_sublobe(prim_freq);   %-- duration of one sublobe, ms
%% natural frequencies
y=(-2:.05:2);    %% Spatial points

x=(-10:.0025:10);    %% frequency points
uu=0;
%% RF pulse parameters

%       for delZ=[1.8 1.4 1.2 1 0.6 0.4 0.2 0.1 0 -0.1 -0.2 -0.4 -0.6 -1
%       -1.2 -1.4 -1.8]
       stype='ms';       %-- spectral profile type     (optional, default 'pm')
       ang=(pi/2);       % -- flip angle, in radians
       tbx=8;            %-- time-bandwidth of spatial profile
       ngx=46;           %-- number of sublobes
       sbw=.2;           %-- spectral bandwidth, kHz
       srip1=0.01;       %-- spectral in-band ripple   (optional, default 0.01)
       srip2=0.01;       % -- spectral stop-band ripple (optional, default 0.01)
       delZ=0;           %Slice offset in cm
       omega=400;        %Precessional frequency
       Trise=0.10;       % Rise time in msec
       thk=0.3;          %slice thickness in cm
%% My gradients design
gmax=calc_gmax(thk,tbx,tgx); %calculating Gss for known slice thickness
grate=gmax/Trise;
addpath(genpath('.'))
[gx,g1,dt]=gradsimulation(tgx,Trise,gmax);
g=gx;
%% Generation of gradient cycle
  gtemp=[g -g];    %simulating gradient cycle with both lobes symmetric
%  gtemp=[g -g1];   %simulating gradient cycle with -ve love asymmetric
```

```
%  gtemp=[g g];     %to be used when constant gradient is
%  used,corresponding
                % changes in gradient generation m file
l1=length(gtemp);
cycling_factor=(ngx)/2;
   if mod((ngx),2)==0
      Gss1=repmat(gtemp,1,cycling_factor);

      Gss=Gss1*2*pi*4.257*dt;
   else
      G1=repmat(gtemp,1,cycling_factor);
      Gss1=[G1 g];
      Gss=Gss1*2*pi*4.257*dt;
   end
%  Gss=4*ones(1,length(rf))*2*pi*4.257*dt; % for constant gradient of 4G/cm
om=ones(1,length(Gss))*2*pi*dt;
% Y=t2hz(x,ngx*tgx);
% X=gt2cm(y,3,ngx*tgx);
%  plot(Gss1);
%%
%stype={'ms';'min';'ls'};
% for dd=1:length(stype)
%     for ang=[pi/90 pi/36 pi/22.5 pi/18 pi/12 pi/6 pi/4 pi/3 5*pi/12 pi/2 pi*0.5833 0.6667*pi 0.75*pi
0.833*pi pi*0.8611 0.9167*pi pi*0.9611 pi*0.9722 pi]
%% Rf generation
uu=uu+1;
rf = dzepse(ang,g,tbx,tgx,ngx,sbw,srip1,srip2,stype);



 %% simulating real and imaginary together
%  phi=atan(imag(rf)./real(rf));
% for mm=1:length(rf);
%     if phi(mm)<0
%      B(mm)=-1*abs(rf(mm));
%     else
%        B(mm)=abs(rf(mm));
%     end
% %     B(x)=A(x,1);
% end
% plot(B);
%% delaying rf with respect to gradients
B=zeros(1,length(g));
% rf= horzcat(B,B,rf);
%rf=[B B B B rf];
%%  rf  during positive gradient lobe only
% xx=1;
% for c= 1:ngx
%     for r=(1+length(g)*(xx-1)):(length(g)*xx);
%        if mod(c,2)==0
%           newrf(r)=0;
%        else
```

```
%            newrf(r)=rf(r);
%        end
%    end
%    xx=xx+1;
% end
% % plot(real(newrf));
% rf=newrf;
%% normalization of rf to tip angle and scaling it to gauss and plotting rf
rf_norm=ang*((rf)/sum((rf)));              %normalization of rf to tip angle
rfs=rf/(2*pi*4.257*dt);                %scaling rf to gauss
 rfs_norm=ang*(rfs/sum(rfs));              %normalization of scaled rf to tip
% angle
 figure('Color',[1 1 1]);
 q=0:(tgx*(ngx))/length(rfs):((tgx*(ngx))-(tgx*(ngx))/length(rfs));
plot(q,real(rf_norm));
xlabel('time in ms');ylabel('rf amplitude in gauss');
grid on
%% adding phase to rf for shifting of slice
 k=zeros(1,length(Gss));
rfshift=zeros(1,length(Gss));
%    for w=1:length(Gss);
%    kk(w)=-(sum(squeeze(Gss(w:end))));      %k-space trajectory
%    rfshift1(w)=exp(1i*kk(w)*delZ)*rf_norm(w);
%    end
     k=-cumsum(Gss);
     rfshift=exp(1i*k.*delZ).*rf_norm;
t=0:(tgx*(ngx))/length(Gss):((tgx*(ngx))-(tgx*(ngx))/length(Gss));
figure;
plot(t,k);
axis off
figure('Color',[1 1 1]);
layerplot(t,Gss1,t,real(rfshift),{'time(ms)';'Gradient Amplitude(G/cm)';'Rf
amplitute(G)'},[0,tgx*ngx;min(Gss1)-0.5,max(Gss1)+0.5]);

%% Simulation of Slice profiles and plotting them
% Mxy=ab2ex(abr(rfshift,Gss,y));
 Mxy=ab2ex(abr(rfshift,Gss+1i*om,y,x));
 I=abs(Mxy(41,:));
%Mxy=ab2ex(abr(rf,ones(length(rf)),y,x));
xppm=x/(omega/1000);
% figure('Color',[1 1 1]);
% plot(y,abs(Mxy));
% figure('Color',[1 1 1]);
% colormap(jet)
% plot(xppm,I);
% figure;
% imagesc(xppm,y,flipdim(abs(Mxy),2),[0 1]);
% set(gca,'XDir','reverse');
% set(gca,'XTick',min(xppm):max(xppm));
% xlabel({'<------';'ppm'})
% ylabel('z(cm)')
% colorbar
```

```
figure('Color',[1 1 1]);
% subplot(2,1,1);
 mesh(xppm,y,flipdim(abs(Mxy),2));
 set(gca,'XDir','reverse');
 set(gca,'XTick',min(xppm):max(xppm));
 colormap(jet)
% freezeColors;
%figure('Color',[1 1 1]);
figure;
% subplot(2,1,2);
 imshow(xppm,y,abs(Mxy), [0 1]);
 axis on
%  set(gca,'XTick',min(xppm):max(xppm));
 set(gca,'YTick',min(y):max(y));
 daspect([1 1 1]);
 xlabel('ppm')
 ylabel('z(cm)')
 colormap(jet)
% freezeColors;
% freezeColors(colorbar);
figure('Color',[1 1 1]);
contour(xppm,y,flipdim(abs(Mxy),2),6);
set(gca,'XDir','reverse');
xlabel({'<------';'ppm'})
ylabel('z(cm)')
colorbar
daspect([1 1 1])
set(gca,'XMinorTick','on');
set(gca,'XTick',[min(xppm):max(xppm)]);
 figure;
 plot(y,abs(Mxy(:,61)));
 xlabel('cm');ylabel('absMxy')
%% Calculation of Maximum value of Mxy
% AAA=size(Mxy);
% abs_Mxy_center(uu,1)=ang*(180/pi);
% abs_Mxy_center(uu,2)=abs(Mxy((AAA(1,1)+1)/2,(AAA(1,2)+1)/2));
% % abs_Mxy_center=abs(Mxy((AAA(1,1)+1)/2,(AAA(1,2)+1)/2));
% maxabs_Mxy(uu,1)=ang*(180/pi);
% maxabs_Mxy(uu,2)=max(abs(Mxy(:)));
% % maxabs_Mxy(uu,3)=stype;
% %maxabs_Mxy=max(abs(Mxy(:)));
% [idx,idy]=find(abs(Mxy)==maxabs_Mxy(uu,2));
% %[idx,idy]=find(abs(Mxy)==maxabs_Mxy);
%     if length(idx)==2
%         id_x(uu,1)=idx(1,1);
%         id_x(uu,2)=idx(2,1);
%         id_y(uu,1)=idy(1,1);
%         id_y(uu,2)=idy(2,1);
%     else
%         id_x(uu,1)=idx;id_x(uu,2)=0;
%         id_y(uu,1)=idy;id_y(uu,2)=0;
%     end
```

```
% end
% end
%        xlswrite('abs_max_Mxy.xls',maxabs_Mxy,'maxabs_Mxy');
%        xlswrite('Mxy_center.xls',abs_Mxy_center,'abxmxy_center');
%        %xlswrite('maxabsMxy_xlocation.xlsx',id_x);
%        %xlswrite('maxabsMxy_ylocation.xlsx',id_y);
%

   %% Making of Text file for the RF pulse
    sf=1023/max(abs(rfshift));                    % scaling factor
    rf_scaled=sf*abs(rfshift);                   % just to have bigger RF values not required though
% dlmwrite('rftextfile_real.txt',real(rf),'\n');    % writing real values of Rf on a text file
% dlmwrite('rftextfile_abs.txt',abs(rf),'\n');      % writing abs values of Rf on a text file
% real_rf=textread('rftextfile_real.txt');                %reading real Rf values in matrix A
% abs_rf=textread('rftextfile_abs.txt');                  %reading abs Rf
% values in a matrix C
final_rf=zeros(length(rf_scaled),3);
for nn=1:length(rf_scaled)
    final_rf(nn,1)=floor(((angle(rfshift(nn)))*180/pi));
    final_rf(nn,2)=(abs((rf_scaled(nn))))-mod((abs((rf_scaled(nn)))),0.001);
    final_rf(nn,3)=1;
    end
dlmwrite('20_0_min1_2.3A.RF',final_rf,'\t');
type 20_0_min1_2.3A.RF
%% simulation of the RF file generated above(just to check)
%  A=textread('4_0_ms_2.3.RF');
% g1=zeros(length(A),1);
% B=zeros(length(A),1);
% for x= 1:length(A)
%    g1(x)=A(x,2);
%    g1(x)=real(g1(x));
%    B(x)=A(x,1);
%    g2(x)=g1(x)*exp(1i*B(x)*(pi/180));
% end
% x=0:(length(A)-1);
% figure
% plot(x,g2)
```

Related Functions

function dzepse (http://www.stanford.edu/~pauly/)

function ab2ex (http://www.stanford.edu/~pauly/)

function abr (http://www.stanford.edu/~pauly/)

```
function [G1,G2,dt]=gradsimulation(Tend,Trise,Gmax)
clc
% close all
%% simulation of oscillating gradient
```

```
% Tend                    %Time for one gradient cycle in msec
% Trise                   % Ramp time(msec)
% Gmax                    %in G/cm for a known slice thickness
SR=Gmax/Trise;
dt=0.004;                %Number of samples along time scale(4us)
Tplat=(Tend-(2*Trise));      %plateau time of the gradient lobe
t=0.004:dt:Tend;
G1=zeros(1,length(t));

%% generating +ve gradient lobe
for n=1:length(t);
      if (t(n)<Trise)
%           G(n)=Gmax;
           G1(n)=SR*t(n);
      elseif t(n)>=Trise && t(n)<=(Tplat+Trise)

           G1(n)=Gmax;
      elseif t(n)>(Tplat+Trise) && t(n)<=(Tend)
%           G(n)=Gmax;
           G1(n)=Gmax-(SR*(t(n)-(Tplat+Trise)));

      end
end
%  figure;
%    plot(G1)
%% for creating asymmetric -ve gradient lobe
Trise=Trise;
SR=Gmax/Trise;
Tplat=(Tend-(2*Trise));      %plateau time of the gradient lobe
t=0.01:dt:Tend;
G2=zeros(1,length(t));
for n=1:length(t);
      if (t(n)<Trise)
%           G(n)=Gmax;
          G2(n)=SR*t(n);
      elseif t(n)>=Trise && t(n)<=(Tplat+Trise)

          G2(n)=Gmax;
      elseif t(n)>(Tplat+Trise) && t(n)<=(Tend)
%           G(n)=Gmax;

          G2(n)=Gmax-(SR*(t(n)-(Tplat+Trise)));

      end
end
% Ggrad=lobes*length(G);
% figure;
%  plot(t,G2);
  %% generating negative gradient lobe
%gradient lobe has symmetry about length(t)/2
% n=floor(length(t)/2)+1;
% offset=1:floor(length(t)/2);
```

```
% G(n+offset)=-(G(n-offset));
% %
%
 %% creating gradient cycle
% gtemp=[G -G];
%  cycling_factor=lobes/2;
% Gcycle=repmat(gtemp,1,cycling_factor);
% tcycle=0:stepsize:(length(Gcycle)-1)*stepsize;
% % if display_en==1
% plot(t,G);
% grid on
% figure
% plot(tcycle,Gcycle);
% grid on
% xlabel('------------> time in mSec')
% ylabel('------------> Apmplitude in mT/m')
% title('Gradient cycle')
%%
% k=zeros(1,length(G));
% for y=1:length(G);
%     l=0.01*G(y);
%     k(y)=l;
%
% end
% plot(k);
end

function [Gmax]=calc_gmax(thk,tbx,tgx)


% function calculates value of Gss required for a given slice thickness
%thk is slice thickness in cm
%tbx is time bandwidth product of subpulse
%tgx is duration of one sub lobe in ms



bw=tbx/tgx;
Gmax=bw/(4.257*thk);
End
```

REFERENCES

1. American Cancer Society. Cancer Facts & Figures 2010.
2. Brown JM, Giaccia AJ. The unique physiology of solid tumors: opportunities (and problems) for cancer therapy. Cancer Res 1998;58(7):1408-1416.
3. Endrich B, Reinhold HS, Gross JF, Intaglietta M. Tissue perfusion inhomogeneity during early tumor growth in rats. J Natl Cancer Inst 1979;62(2):387-395.
4. Dewhirst MW, Tso CY, Oliver R, Gustafson CS, Secomb TW, Gross JF. Morphologic and hemodynamic comparison of tumor and healing normal tissue microvasculature. Int J Radiat Oncol Biol Phys 1989;17(1):91-99.
5. Grunt TW, Lametschwandtner A, Staindl O. The vascular pattern of basal cell tumors: light microscopy and scanning electron microscopic study on vascular corrosion casts. Microvasc Res 1985;29(3):371-386.
6. Shah-Yukich AA, Nelson AC. Characterization of solid tumor microvasculature: a three-dimensional analysis using the polymer casting technique. Lab Invest 1988;58(2):236-244.
7. Zhao D, Jiang L, Mason RP. Measuring changes in tumor oxygenation. Methods Enzymol 2004;386:378-418.
8. Brown JM. The hypoxic cell: a target for selective cancer therapy--eighteenth Bruce F. Cain Memorial Award lecture. Cancer Res 1999;59(23):5863-5870.
9. Vaupel P, Harrison L. Tumor hypoxia: causative factors, compensatory mechanisms, and cellular response. Oncologist 2004;9 Suppl 5:4-9.
10. Tatum JL, Kelloff GJ, Gillies RJ, Arbeit JM, Brown JM, Chao KS, Chapman JD, Eckelman WC, Fyles AW, Giaccia AJ, Hill RP, Koch CJ, Krishna MC, Krohn KA, Lewis JS, Mason RP, Melillo G, Padhani AR, Powis G, Rajendran JG, Reba R, Robinson SP,

Semenza GL, Swartz HM, Vaupel P, Yang D, Croft B, Hoffman J, Liu G, Stone H, Sullivan D. Hypoxia: importance in tumor biology, noninvasive measurement by imaging, and value of its measurement in the management of cancer therapy. Int J Radiat Biol 2006;82(10):699-757.

11. Harris AL. Hypoxia--a key regulatory factor in tumour growth. Nat Rev Cancer 2002;2(1):38-47.
12. Sartorelli AC. Therapeutic attack of hypoxic cells of solid tumors: presidential address. Cancer Res 1988;48(4):775-778.
13. Teicher BA, Lazo JS, Sartorelli AC. Classification of antineoplastic agents by their selective toxicities toward oxygenated and hypoxic tumor cells. Cancer Res 1981;41(1):73-81.
14. Brown JM, Wilson WR. Exploiting tumour hypoxia in cancer treatment. Nat Rev Cancer 2004;4(6):437-447.
15. Gray LH, Conger AD, Ebert M, Hornsey S, Scott OC. The concentration of oxygen dissolved in tissues at the time of irradiation as a factor in radiotherapy. Br J Radiol 1953;26(312):638-648.
16. Kodibagkar VD, Wang X, Mason RP. Physical principles of quantitative nuclear magnetic resonance oximetry. Front Biosci 2008;13:1371-1384.
17. Stone HB, Brown JM, Phillips TL, Sutherland RM. Oxygen in human tumors: correlations between methods of measurement and response to therapy. Summary of a workshop held November 19-20, 1992, at the National Cancer Institute, Bethesda, Maryland. Radiat Res 1993;136(3):422-434.
18. Vaupel P, Schlenger K, Knoop C, Hockel M. Oxygenation of human tumors: evaluation of tissue oxygen distribution in breast cancers by computerized O2 tension measurements. Cancer Res 1991;51(12):3316-3322.

19. Bussink J, Kaanders JH, Strik AM, Vojnovic B, van Der Kogel AJ. Optical sensor-based oxygen tension measurements correspond with hypoxia marker binding in three human tumor xenograft lines. Radiat Res 2000;154(5):547-555.

20. Griffiths JR, Robinson SP. The OxyLite: a fibre-optic oxygen sensor. Br J Radiol 1999;72(859):627-630.

21. Rajendran JG, Krohn KA. Imaging hypoxia and angiogenesis in tumors. Radiol Clin North Am 2005;43(1):169-187.

22. Padhani AR, Krohn KA, Lewis JS, Alber M. Imaging oxygenation of human tumours. Eur Radiol 2007;17(4):861-872.

23. Koh WJ, Rasey JS, Evans ML, Grierson JR, Lewellen TK, Graham MM, Krohn KA, Griffin TW. Imaging of hypoxia in human tumors with [F-18]fluoromisonidazole. Int J Radiat Oncol Biol Phys 1992;22(1):199-212.

24. Cook GJ, Houston S, Barrington SF, Fogelman I. Technetium-99m-labeled HL91 to identify tumor hypoxia: correlation with fluorine-18-FDG. J Nucl Med 1998;39(1):99-103.

25. Howe FA, Robinson SP, McIntyre DJ, Stubbs M, Griffiths JR. Issues in flow and oxygenation dependent contrast (FLOOD) imaging of tumours. NMR Biomed 2001;14(7-8):497-506.

26. Swartz HM, Dunn JF. Measurements of oxygen in tissues: overview and perspectives on methods. Adv Exp Med Biol 2003;530:1-12.

27. Glockner JF, Swartz HM. In vivo EPR oximetry using two novel probes: fusinite and lithium phthalocyanine. Adv Exp Med Biol 1992;317:229-234.

28. Gallez B, Swartz HM. In vivo EPR: when, how and why? NMR Biomed 2004;17(5):223-225.

29. Gallez B, Baudelet C, Jordan BF. Assessment of tumor oxygenation by electron paramagnetic resonance: principles and applications. NMR Biomed 2004;17(5):240-262.

30. Mason RP. Non-invasive physiology: 19F NMR of perfluorocarbons. Artif Cells Blood Substit Immobil Biotechnol 1994;22(4):1141-1153.

31. Mason RP, Rodbumrung W, Antich PP. Hexafluorobenzene: a sensitive 19F NMR indicator of tumor oxygenation. NMR Biomed 1996;9(3):125-134.

32. Kodibagkar VD, Wang X, Pacheco-Torres J, Gulaka P, Mason RP. Proton imaging of siloxanes to map tissue oxygenation levels (PISTOL): a tool for quantitative tissue oximetry. NMR Biomed 2008;21(8):899-907.

33. De Graaf RA. In vivo NMR spectroscopy: principles and techniques. 2nd ed: Wiley; 2008.

34. Bottomley PA, Hardy CJ. Two-Dimensional Spatially Selective Spin Inversion and Spin-Echo Refocusing with a Single Nuclear-Magnetic-Resonance Pulse. Journal of Applied Physics 1987;62(10):4284-4290.

35. Pauly J, Nishimura D, Macovski A. A K-Space Analysis of Small-Tip-Angle Excitation. Journal of Magnetic Resonance 1989;81(1):43-56.

36. Pauly J, Spielman D, Macovski A. Echo-Planar Spin-Echo and Inversion Pulses. Magnetic Resonance in Medicine 1993;29(6):776-782.

37. Meyer CH, Pauly JM, Macovski A, Nishimura DG. Simultaneous spatial and spectral selective excitation. Magn Reson Med 1990;15(2):287-304.

38. Kodibagkar VD, Cui W, Merritt ME, Mason RP. Novel 1H NMR approach to quantitative tissue oximetry using hexamethyldisiloxane. Magn Reson Med 2006;55(4):743-748.

39. Markley JL, Horsley WJ, Klein MP. Spin-Lattice Relaxation Measurements in Slowly Relaxing Complex Spectra. Journal of Chemical Physics 1971;55(7):3604-&.

40. Gulaka P, Rastogi U, Mckay M, Wang X, Mason RP, Kodibagkar VD. Hexamethyldisiloxane based nanoprobes for ^{1}H MRI oximetry. NMR in Biomedicine 2010;under review.

41. Pauly JM. RF pulse design for magnetic resonance imaging [http://www.stanford.edu/~pauly/].

42. Sharma SK, Lowe KC, Davis SS. Emulsification Methods for Perfluorochemicals. Drug Development and Industrial Pharmacy 1988;14(15-17):2371-2376.

BIOGRAPHICAL INFORMATION

Ujjawal Rastogi completed his Bachelor of Engineering in Biomedical Engineering in June 2007 from Mahatma Gandhi Mission's College of Engineering and Technology, Navi Mumbai, India. During his undergraduate degree he did research work at prestigious Bhabha Atomic Research Center (BARC) and was a part of the team that developed a non-invasive blood glucose monitor. In August 2008 he joined University of Texas at Arlington to pursue Master of Science degree in Biomedical Engineering. In Fall 2009 he was awarded scholarship of $1000 for outstanding performance by the Department of Bioengineering at University of Texas at Arlington. He joined Dr. Kodibagkar's MR lab at University of Texas Southwestern Medical Center, Dallas, USA in September 2009 and followed his research interest in Magnetic Resonance Imaging and its applications.